

## ARTICLE

## Covalent Organic Framework Photocatalysts: Structures and Applications

Received 00th January 20xx,  
Accepted 00th January 20xx

Han Wang,<sup>†a</sup> Hui Wang,<sup>†b</sup> Ziwei Wang,<sup>†a</sup> Lin Tang,<sup>†a</sup> Guangming Zeng,<sup>\*a</sup> Piao Xu,<sup>\*a</sup> Ming Chen,<sup>a</sup> Ting Xiong,<sup>a</sup> Chengyun Zhou,<sup>a</sup> Xiyi Li,<sup>b</sup> Danlian Huang,<sup>a</sup> Yuan Zhu,<sup>a</sup> Zixuan Wang<sup>a</sup> and Junwang Tang<sup>\*b</sup>

DOI: 10.1039/x0xx00000x

With the increasing energy demands and environmental pollution, to find a clean and renewable energy source is in urgent need. In these years, photocatalysis that uses solar energy for either fuel production, such as hydrogen evolution and hydrocarbon production, or environmental pollutant degradation, has shown a great potential to achieve this goal. Among the various photocatalysts, covalent organic frameworks (COFs) are very attractive due to their excellent structural regularity, robust **framework**, inherent porosity and good activity. Thus, many studies have been carried out to investigate the photocatalytic performance of COFs and COF-based photocatalysts. In this critical review, the recent progress and advances of COF photocatalysts are thoroughly presented. Furthermore, diverse links between COF building blocks such as boron-containing connections and nitrogen-containing connections are summarized and compared. The morphologies of COFs and several commonly used strategies pertaining to photocatalytic activity are also discussed. Following this, the applications of COF-based photocatalysts are detailed including photocatalytic hydrogen evolution, CO<sub>2</sub> conversion and degradation of environmental contaminants. Finally, a summary and perspective on the opportunities and challenges for the future development of COF and COF-based photocatalysts is proposed.

## 1. Introduction

With the rapid industrialization and urbanization, there has never been a greater concern towards the sustainable supply of fossil fuels (e.g. oil, coal and gas) and the severe environmental issues caused by utilization of these fossil fuels.<sup>1–3</sup> Thus, it is urgent to secure an alternative, sustainable, clean energy source by an effective and scalable technology to address the environment and energy issues. Solar driven chemical processes including water splitting, CO<sub>2</sub> conversion, photocatalytic degradation, etc., have attracted substantial interest because of solar energy as an abundant and inexhaustible source. The method to utilize solar energy is denoted as photocatalysis in which the electron from the valence band (VB) can be excited to the conduction band (CB) when the energy of photons is greater than the semiconductor band gap, creating the electron/hole pairs in the photocatalysts, and the separated electrons and holes migrate to the surface to participate in the chemical reactions.

In 1970's, Fujishima and Honda realized the water splitting under ultraviolet (UV) radiation by using titanium dioxide (TiO<sub>2</sub>) electrode for the first time.<sup>4</sup> And Carey et al. carried out the

photocatalytic degradation of organic pollutants with TiO<sub>2</sub> in aqueous suspensions four years later.<sup>5</sup> These have sparked intense interest among researchers for artificial photosynthesis. Traditional inorganic semiconductor photocatalysts such as TiO<sub>2</sub>,<sup>6–8</sup> cadmium sulfide (CdS),<sup>9–11</sup> zinc oxide (ZnO)<sup>12, 13</sup> and silver phosphate (Ag<sub>3</sub>PO<sub>4</sub>)<sup>14</sup> have occupied a leading position over the past several decades. Among them, TiO<sub>2</sub> is the most important and well-known photocatalyst due to its low cost, relatively high availability and durability. However, its wide band gap of 3.2 eV that only allows for ultraviolet light absorption limits its utilization of solar spectrum, leading to the low photocatalytic efficiency and photocurrent quantum yield.<sup>15</sup> Besides, Ag<sub>3</sub>PO<sub>4</sub>, CdS and other transition metal sulfides and oxides with suitable band gap to absorb visible light and good carrier transportation capacity have stimulated the attention of the photocatalytic studies, whereas the heavy metal toxicity and photo-corrosion effect block their practical applications.<sup>9</sup> As the research progressed, organic semiconductors like graphitic carbon nitride (g-C<sub>3</sub>N<sub>4</sub>),<sup>16, 17</sup> metal-organic frameworks (MOFs),<sup>18, 19</sup> and covalent organic frameworks (COFs)<sup>20–24</sup> have been used as the photocatalyst and show promising performance towards solar energy conversion. g-C<sub>3</sub>N<sub>4</sub> as a metal-free polymer possesses many fascinating features including “earth-abundant” nature, high physicochemical stability and favorable band gap structure. However, the drawbacks exist that their synthesis is often conducted at the high temperature (> 500 °C) and their molecular backbone consists of either triazine or heptazine units, leading to the limited structural diversity.<sup>25</sup> As a type of porous crystalline materials, MOFs constructed from organic linkers and transition-metal nodes are attractive due to their large surface area, structural tailorability and easy pore functionalization. Unfortunately, most MOFs are instable and can easily be deteriorated under humid conditions which causes the problem of repeated use.<sup>19</sup>

<sup>a</sup> College of Environmental Science and Engineering, Hunan University and Key Laboratory of Environmental Biology and Pollution Control (Hunan University), Ministry of Education, Changsha 410082, P. R. China. E-mail: [zgming@hnu.edu.cn](mailto:zgming@hnu.edu.cn); [piaoxu@hnu.edu.cn](mailto:piaoxu@hnu.edu.cn).

<sup>b</sup> Department of Chemical Engineering, University College London, Torrington Place, London, WC1E7JE, UK. E-mail: [junwang.tang@ucl.ac.uk](mailto:junwang.tang@ucl.ac.uk).

<sup>†</sup> These authors contribute equally to this article.

Electronic Supplementary Information (ESI) available: [details of any supplementary information available should be included here]. See DOI: 10.1039/x0xx00000x

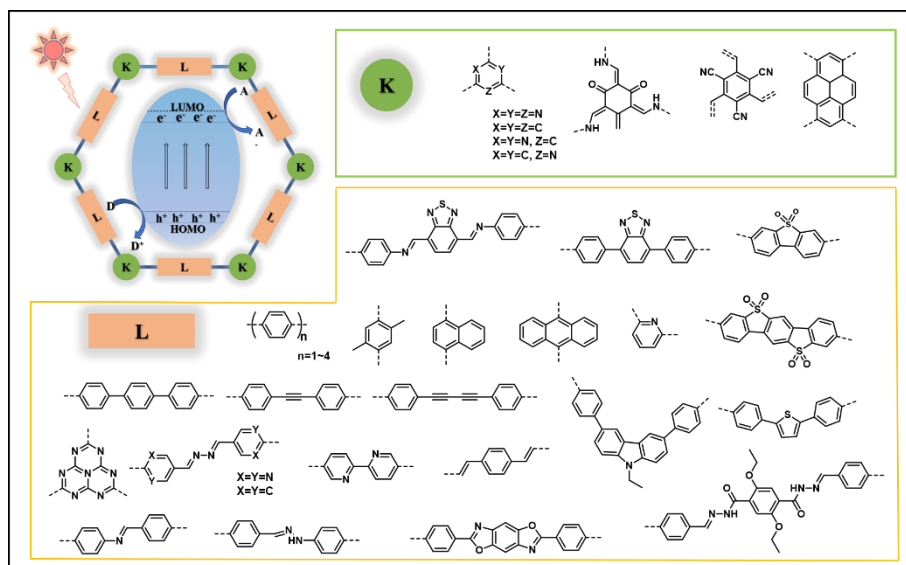


Fig. 1 Structures of COF photocatalysts. (K represents knots; L represents linkers)

Covalent organic frameworks (COFs), as a newly developed organic polymer, have caused ripples of excitement among researchers striving to exploit their promising photocatalytic potentials. COFs with low density are crystalline porous materials composed of organic molecules linked by covalent bond through reticular chemistry, which have been widely used in areas such as heterogeneous catalysts,<sup>26-29</sup> gas storage and separation,<sup>30,31</sup> energy storage and optoelectronic devices.<sup>32-34</sup> Compared with traditional semiconductors, COFs possess not only some common features but also many special advantages pertaining to photocatalysis: i) the structural designability of COFs enables them to realize the design of targeted structures and special properties related to photocatalytic reactions such as excellent visible-light absorption, fast electron-hole separation and transfer; ii) the large surface area of COFs provides the accessible catalytic sites, and the highly crystalline and porous structures endow COFs with accelerated charge transport to the surface, decrease the possibility of charge trapping caused by defects, thus contributing to the suppressed electron-hole recombination; iii) COFs with strong covalent band show high chemical and thermal stability, and photoactive units fixed in the robust framework can avoid photo-corrosion and enhance the lifetimes of the excited states; iv) the extended  $\pi$ -conjugated structure both in plane and the stacking direction enables the high charge carrier mobilities. These fascinating inherent features endow COFs with great potential in photocatalytic energy conversion and environmental remediation, which are deemed to match or even exceed MOFs and conventional photocatalytic semiconductors. Lotsch and co-workers reported the first discovery of COF in photocatalysis.<sup>35</sup> A high visible-light-induced hydrogen production efficiency has been achieved based on hydrazine-based TFPT-COF (evolution rate:  $1970 \mu\text{mol h}^{-1} \text{g}^{-1}$ , triethanolamine (TEOA) as a sacrificial donor), which was competitive with other representative photocatalysts including Pt-modified amorphous melon ( $720 \mu\text{mol h}^{-1} \text{g}^{-1}$ ), g-C<sub>3</sub>N<sub>4</sub> synthesized at  $600^\circ\text{C}$  ( $840 \mu\text{mol h}^{-1} \text{g}^{-1}$ ),<sup>36</sup> and crystalline poly(triazine imide) ( $864 \mu\text{mol h}^{-1} \text{g}^{-1}$ ).<sup>37</sup> This success has initiated the exploration of COF-based photocatalysts in the whole community (Fig. 1).

The number of publications in the area of COF-based photocatalysts has increased sharply, a comprehensive review of COF photocatalyst is needed. In this review, we began by

summarizing different connections of COF building blocks including boron-containing connections, nitrogen-containing connections and double-stage connections combining imine linkages and boronate ester linkages. Subsequently, we compared the performance of COFs over different morphologies, such as 0-dimensional (0D) nanoparticles, 1-dimensional (1D) nanofibers and nanowires, 2-dimensional (2D) thin films and nanosheets, and 3-dimensional (3D) hollow structures. Strategies related to the enhanced photocatalytic performance of COF materials were then presented. Afterwards, the solar-driven application of COFs was discussed, including water splitting, CO<sub>2</sub> conversion as well as photocatalytic degradation of pollutants in wastewater. Finally, a perspective on the challenges and opportunities in this area, including synthesis, functions and application, was discussed. Complementary to this review, audience are also suggested to read another review about design of COF if they are interested in the materials design.<sup>38-44</sup>

## 2. Linking chemistry of COFs

COFs are a kind of crystalline porous materials with pure organic groups connected by robust covalent bonds. Diverse covalent bonds formed from various synthetic organic reactions between theoretically unlimited building blocks endow COFs with designable crystalline structures and targeted functions. In this section, different linkages of COF building blocks were summarized, including boron-containing linkage, triazine linkage, imine linkage,  $\beta$ -ketoenamines linkage, hydrazones and azines linkages, and other linkages (Fig. 2).

### 2.1. Boron-containing linkage

Since the pioneering research of Yaghi and co-workers that constructed the first two COFs, namely COF-1 and COF-5, diverse syntheses of COFs linked by boron-containing linkages via the formation of boronate ester, boroxine or borazine have generated considerable interest.<sup>45</sup> The most synthesized boron-based COFs could be clarified into two categories: single building block self-condensation and two or more building units co-condensation.

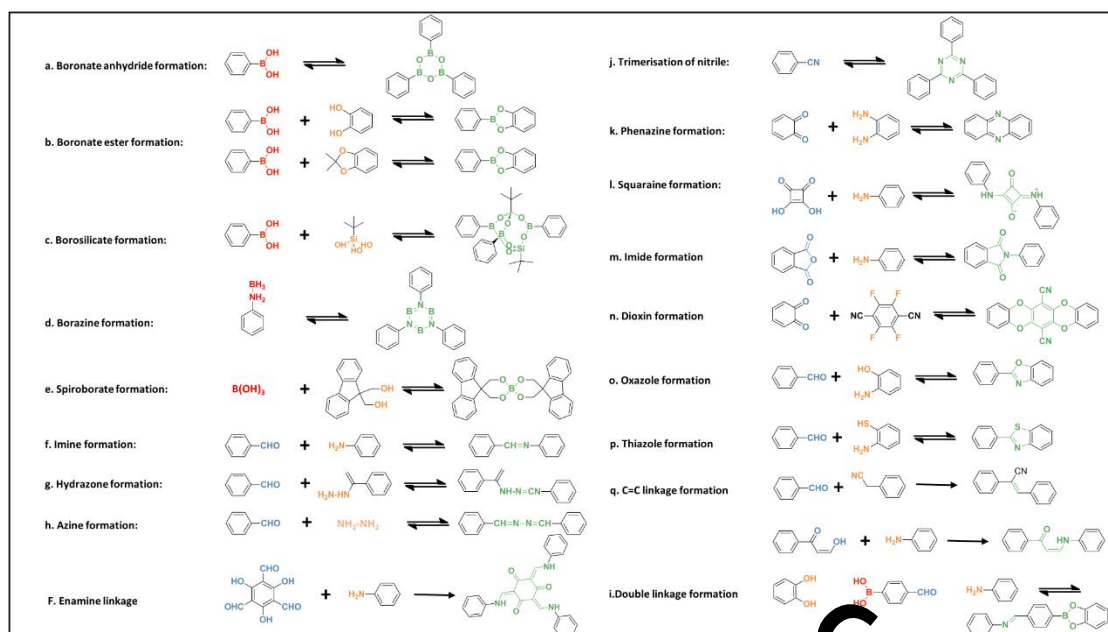


Fig. 2 Various linkages of COFs formation.

As a representative example, COF-1 was designed and fabricated through the self-condensation of 1, 4-benzenediboric acid (BDDBA), which was based on the molecular dehydration to form six-membered boroxine connections.<sup>45</sup> The as-prepared COF-1 possessed a layered graphitic structure with the hexagonal pores diameter of 15 Å and a Brunauer-Emmett-Teller (BET) surface area of 711 m<sup>2</sup> g<sup>-1</sup>. In this method, it is essential to keep the reaction under a closed condition for water equilibrium to guarantee the reversibility in COF formation. Similarly, the same group further successfully constructed the first 3D COFs (COF-102 and COF-103) with the self-condensation of the tetrahedral molecular building blocks tetra(4-dihydroxyborylphenyl)methane (TBPM) or its planar analog (TBPS).<sup>46</sup> The crystalline COF-102 and COF-103 exhibited a higher BET surface area of 3472 m<sup>2</sup> g<sup>-1</sup> and 4210 m<sup>2</sup> g<sup>-1</sup>, respectively. Since then, this self-condensation strategy has been widely used to fabricate boron-containing COFs based on various monomers, such as biphenyldiboric acid,<sup>47</sup> pyrene-2,7-bis(boric acid) (PDA),<sup>48</sup> and 4, 4'-phenylazobenzoyl diboric acid.

Besides self-condensation, the co-condensation of two or more building blocks such as boronic acids with catechols has also been reported. The dehydration condensation of 2, 3, 6, 7, 10, 11-hexahydroxytriphenylene (HHTP) and BDDBA resulted in the formation of layered COF-5 with five-membered BO<sub>2</sub>C<sub>2</sub> rings, which exhibited an eclipsed boron nitride arrangement.<sup>45</sup> It is worth mentioning that COF-5 has been widely regarded as a representative to examine various newly synthesis strategy.<sup>50-52</sup> Likewise, the first crystalline boronate-linked 3D COFs (COF-105 and COF-108) were obtained by replacing BDDBA with tetrahedral molecules TBPM and TBPS, respectively.<sup>46</sup> COFs with different properties and functions could be designed and synthesized by a diverse combination of building units. For instance, a novel photoactive donor-acceptor TP-Por COF was prepared based on triphenylene and porphyrin units.<sup>53</sup> The resulting TP-Por COF film with enhanced charge separation

showed a broad optical absorption covering the entire visible range up to 680 nm. In a conventional condensation, donor-acceptor D<sub>TP</sub>-A<sub>NDI</sub>-COF with the large pore size of 5.3 nm was obtained from N,N'-di-(4-borono-2-phenyl)naphthalene-1,4,5,8-tetracarboxylic acid diimide and HHTP.<sup>54</sup> The charge-separation state lifetime of 2.5 μs was determined by time-resolved electron spin resonance spectroscopy, indicating the presence of long-lived radicals produced through the effective charge transfer from donor triphenylene to acceptor naphthalene diimide. Notably, polyfunctional catechols are easy to oxidation and hard to dissolve in most organic solvents, leading to difficulty fabrication of functional building blocks and related COFs. Thus, a new Lewis acid-catalyzed strategy protecting catechols from oxidation was put forward.<sup>55</sup> Boronate ester-linked Pc-PBBA COF with a pore size of 2.3 nm was constructed from 1,4-phenylenebis(boronic acid) (PBBA) and phthalocyanine tetra(acetonide) (Pc) in the presence of Lewis-acid catalyst BF<sub>3</sub>•OEt<sub>2</sub>. The as-prepared eclipsed COF with broad absorbance showed great potential for effective charge transfer through the stacked phthalocyanines. In contrast with the conventional condensation of two component, a multiple-component (MC) strategy was also studied.<sup>56</sup> For example, a three-component [1+2] co-condensation was proceeded by using the shortest unit BDDBA and a longer molecule PDA as the linkers to react with HHTP as the knots. Two MC-COFs (termed MC-COF-TP-E<sub>1</sub><sup>1</sup>E<sub>2</sub><sup>2</sup> and MC-COF-TP-E<sub>1</sub><sup>2</sup>E<sub>2</sub><sup>1</sup>) with slipped AA stacking were generated to possess the BET surface area of 1892 and 1534 m<sup>2</sup> g<sup>-1</sup> and pore sizes of 3.2 and 2.9 nm, respectively. This co-condensation strategy could also be used to tailor the functionality of COFs. A highly emissive 2D COF TPE-Ph COF was designed by introducing an aggregation-induced emission active tetraphenylethene (TPE) unit to condense with TPE-cored boronic acids and 1, 2, 4, 5-tetrahydroxybenzene.<sup>57</sup> Considering that the boronate linkages in TPE-Ph COF formed Lewis acid-base pair when

interacted with ammonia, TPE-Ph COF could be used as a fluorescence sensor for ammonia.

Generally, COFs with boron-containing linkages possess low density and high surface area, leading to various applications.<sup>58, 59</sup> However, boroxines and boronate ester are easy to hydrolysis and oxidation, and thereby limiting their application as catalysts or with long-term usage. Still, it is undeniable that boron-containing COFs are of particular importance for mechanistic study.<sup>50, 60, 61</sup>

## 2.2. Triazine-based linkage

In 2008, Thomas and co-workers reported the first example of triazine-based COFs (donated as CTFs), which was achieved by cyclotrimerization of aromatic nitriles at 400 °C with the catalysis of ZnCl<sub>2</sub>.<sup>62</sup> However, harsh synthesis conditions, such as high reaction temperature and acid solution purification, lead to the destruction of long-range order. Only a few crystalline CTFs have been prepared by this method constructed from 1, 3, 5-tricyanobenzene, 1, 4-dicyanobenzene and 2, 6-dicyanonaphthalene monomers, namely CTF-0, CTF-1 and CTF-2, respectively.<sup>63, 64</sup> Moreover, limited building blocks are able to withstand the high reaction temperature, thus lowering the diversity of CTFs. Thus, other strategies based on milder conditions have been developed.<sup>65–67</sup> A low-temperature polycondensation approach was utilized to synthesize CTFs based on a broader range of building blocks under mild conditions.<sup>68</sup> For example, CTF-HUST-1 prepared from 1, 4-benzene-dialdehyde reacted at ambient pressure with a temperature lower than or equal to 120 °C, which also enabled the large scale synthesis. Soon afterward, a new concept was put forward to fabricate highly crystalline CTFs by in-situ oxidizing alcohol to form aldehyde with controlled reaction rates. The principle behind this reaction was that decreasing nucleation rates and lowering the concentration of nucleation could lead to relatively high crystallization.<sup>69</sup> The as-prepared CTFs possessed much-improved crystallinity and higher photocatalytic performance compared to low crystalline or amorphous CTFs, and a controlling feeding rate method was also used to achieve highly crystalline CTFs.<sup>70</sup>

Despite the crystalline problems, high BET surface area, remarkable thermal and chemical stabilities, and controllable C/N/H composition endow CTFs with potential for catalysis. 2D CTFs with triazine subunits can be regarded as analogs of g-C<sub>3</sub>N<sub>4</sub>, which has been studied extensively as photocatalyst.<sup>71, 72</sup> On the one hand, the incorporated nitrogen in backbone benefits for metal nanoparticle loading, which provides a platform for the introduction of the active sites for the catalytic reaction. On the other hand, the tunable structures with unlimited organic subunits allow for the controllable band alignment and optimal light absorption.<sup>73</sup> Studies demonstrated that the photocatalytic hydrogen production of CTF-1 can be varied with different reaction conditions. For example, a well-ordered CTF-1 was synthesized via a mild microwave-assisted condensation.<sup>74</sup> Apparent quantum efficiency (AQE) of 3.8 % and 6 % at 420 nm for oxygen and hydrogen evolution under visible light irradiation was determined, respectively. In particular, the oxygen evolution rate and hydrogen evolution rate of CTF-1-100W were 140 μmol g<sup>-1</sup> h<sup>-1</sup> and 5500 μmol g<sup>-1</sup> h<sup>-1</sup>, respectively, both of which are higher than those of g-C<sub>3</sub>N<sub>4</sub>.<sup>71, 75</sup> The examples verified the promising

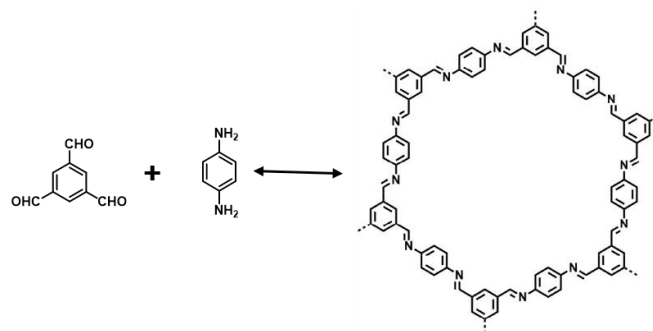


Fig. 3 Schematics for the synthesis of COF-LZU1.

properties and applications of triazine-linked COFs. A successful synthesis of crystalline CTFs with a large scale will be the focus of future research.

## 2.3. Imine linkage

The polymerization of amines and aldehydes leads to the formation of imine bonds. While the resulting layered COFs with imine linkages were similar to boronic ester COFs, the imine-linked COFs showed higher stability to water, which was significantly different from boron-containing COFs. Even though their stability may be also influenced by the incorporated linkers, imine bonds have been one of the most attractive linkage motifs in COFs owing to the plenty obtainable imine and aldehyde linkers as well as the great potential for constructing conjugated  $\pi$ -systems through the COF sheets. To date, imine formation is clearly the most common synthesis strategy employed to build COFs. Early in 2009, the first imine-linked 3D COF (named as COF-300) was reported via the copolymerization of terephthalaldehyde (TA) and tetra-(4-anilyl)methane (TAM) by using 1,4-dioxane as the solvent and aqueous acetic acid as catalyst.<sup>76</sup> The Fourier transform infrared (FT-IR) spectrum of COF-300 exhibited the C=N stretch at 1620 and 1202 cm<sup>-1</sup>, which confirmed the formation of imine bonds. The as-prepared crystalline COF-300 with 5-fold interpenetration was stable up to 490 °C. Furthermore, TAM has been widely used in the construction of 3D COFs.<sup>23, 77, 78</sup> Similarly, the first imine-linked 2D COF COF-LZU1 was synthesized through the condensation of 1, 4-diaminobenzene with 1, 3, 5-triformylbenzene (Fig. 3).<sup>79</sup> The as-prepared COF-LZU1 showed high stability against water and common organic solvent including acetone, dimethyl sulfoxide, tetrahydrofuran, trichloromethane, N,N-dimethylformamide. FT-IR spectrum of COF-LZU1 displayed a strong C=N stretching mode of imines at 1618 cm<sup>-1</sup>. COF-LZU1 was demonstrated to be an ideal platform for metal ions incorporation due to the eclipsed layered-sheet arrangement. Indeed, Pd/COF-LZU1 catalyst was successfully achieved by post-modification of COF-LZU1 with palladium acetate.

Various building blocks have been involved in imine-based COF formation.<sup>80–85</sup> For instance, a highly conjugated  $\pi$ -electron porphyrin unit and its metal derivatives have been largely employed in the construction of functional imine-linked COFs. One study introduced two porphyrin-based COFs, termed COF-66 and COF-366, with the feature of extended planar  $\pi$ -conjugation.<sup>86</sup> COF-66 and COF-366 were obtained from the solvothermal reaction of porphyrin and TA and tetrahydroxy anthracene, respectively, and the formed



imine bond was characterized by FT-IR and  $^{13}\text{C}$  cross-polarization magic-angle spinning (CP-MAS) NMR spectroscopic techniques. Both COFs exhibited high charge carrier mobility owing to the close intermolecular  $\pi$ - $\pi$  distances. A series of porphyrin COFs MP-DHPH COFs with varied H-bonding sites was synthesized via a three-component condensation strategy. Specifically, porphyrin derivatives (MP; M =  $\text{H}_2$ , Cu, and Ni) were used to react with a mixture of TA and dihydroxyterephthalaldehyde (DHTA, H-bonding edges) at different molar ratios. Determined by ultraviolet-visible diffuse reflectance spectroscopy (UV-vis DRS),  $\text{H}_2\text{P-DHPH}$  COF, CuP-DHPH COF, and NiP-DHPH COF possessed narrower band gaps of 1.31, 1.36, and 1.54 eV compared to that of 1.36, 1.40, and 1.58 eV for the corresponding amorphous MP-Ph polymers, respectively. The  $\text{H}_2\text{P-DHPH}$  COF displayed higher photocatalytic singlet oxygen evolution than CuP-DHPH COF and NiP-DHPH COF, and the photocatalytic performance of COFs increased with the increasing content of H-bonding site. More recently, a conjugated imine-linked metalloporphyrin COF was prepared through the Schiff-base reaction of Zn-5,10,15,20-tetrakis(4-aminophenyl)-21H,23H-porphyrin (Zn-TAPP) and Cu-5,10,15,20-tetrakis(4-formylphenyl)-21H,23H-porphyrin (Cu-TFPP) in the presence of *n*-butanol, *o*-dichlorobenzene and aqueous acetic acid. The resulting ZnCu-Por-COF possessed effective  $\pi$ -conjugation and high charge-transfer transition.

Interestingly, COFs with two types of covalent linkage were realized by orthogonal (interference-free) reaction strategy. Binary NTU-COF-1 with both boroxine ring and imine group was constructed from the copolymerization of 1,3,5-tris(4-aminophenyl)-benzene (TAPB) and 4-formylphenylboronic acid (FPBA), in which possessed ditopic units of aldehyde and boronate. As indicated by FT-IR spectra, the appearance of B-O stretching bands ( $1336\text{ cm}^{-1}$  and  $1305\text{ cm}^{-1}$ ), B-C band ( $1221\text{ cm}^{-1}$ ),  $\text{B}_3\text{O}_3$  band ( $711\text{ cm}^{-1}$ ) and a strong C=N band ( $1627\text{ cm}^{-1}$ ) verified the existence of  $\text{B}_3\text{O}_3$  rings and imine linkage. Likewise, ternary NTU-COF-2 was successfully synthesized based on TAPB, FPBA, and HHTP with the formation of  $\text{C}_2\text{B}_2$  boronate ring and imine group. Accordingly, there are two paths for the design of bifunctional linkages. First, one of the building units possess at least two functional moieties, which enables the simultaneous reactions of co-condensation and self-condensation with other functional building blocks, such as TATTA-FPBA COF (TATTA: 4,4',4''-(1,3,5-triazine-2,4,6-triyl)trianiline) and NTU-COF-1.<sup>83</sup> Second, three functional building blocks were employed, and at least one of them has two different functional moieties to enable two non-interfering co-condensation reaction, like NTU-COF-2 and HHTP-FPBA-TATTA COF.<sup>83</sup>

#### 2.4. $\beta$ -ketoenamines linkage

Improving the stability of COFs is of vital importance pertaining to their applications. Banerjee et al. put forward a two-step strategy to fabricate COFs with high stability when subjected to boiling water, acids and strong bases.<sup>87</sup> Specifically, TpPa-1 and TpPa-2 with ketoenamine linkage were realized by the condensation of 1, 3, 5-triformylphloroglucinol (Tp) with *p*-phenylenediamine (Pa-1) or 2,5-dimethyl-*p*-phenylenediamine (Pa-2), in which Tp possess hydroxyl groups adjacent to the formyl groups (Fig. 4). Two steps have been involved in COFs formation that is the crystalline framework formed

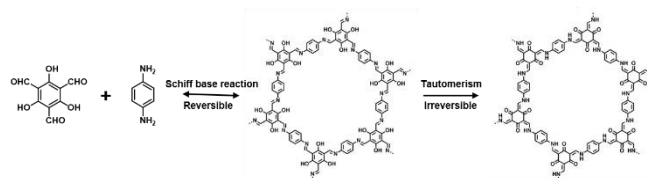


Fig. 4 Schematic illustration of the formation of TpPa which involved the steps of reversible Schiff-base reaction and irreversible enol-to-keto tautomerism.

based on the reversible Schiff base reaction, and enhanced stability originated from irreversible enol-to-keto tautomerization. The structure of as-prepared TpPa-1 and TpPa-2 maintained integrity in boiling water and acid, and TpPa-2 was also stable in a basic medium. Notably,  $\beta$ -ketoenamines linked COFs usually feature less crystalline compared to their imine counterparts as a result of irreversible procedure that error correction might be hindered in COF lattice.<sup>88, 89</sup>

Understandably then, the remarkable chemical stability endows  $\beta$ -ketoenamines linked COFs with exceptional potential for diverse applications such as photocatalytic reaction. Moreover, keto functionalities present in the  $\beta$ -ketoenamine core could help to enhance the lifetime of the excited triplet state.<sup>90</sup> For example, two chemical stable  $\beta$ -ketoenamine COFs were prepared for photocatalytic hydrogen production.<sup>91</sup> The designed TP-EDDA COF bearing acetylene functional groups was constructed from Tp and 4,4'-(ethyne-1,2-diyl)dianiline (EDDA), while Tp-BDDA COF with diacetylene moieties was based on the reaction of Tp and 4,4'-(buta-1,3-diene-1,4-diyl)dianiline (BDDA). The appearance of characteristic signals corresponding to C=C and C-N bonds at  $\sim 1451$  and  $\sim 1251\text{ cm}^{-1}$  confirmed the formation of  $\beta$ -ketoenamine functionalities. A much higher photocatalytic hydrogen evolution rate of TP-BDDA ( $324 \pm 10\text{ }\mu\text{mol h}^{-1}\text{ g}^{-1}$ ) was observed compared to that of TP-EDDA ( $30 \pm 5\text{ }\mu\text{mol h}^{-1}\text{ g}^{-1}$ ). Similarly, thioether-functionalized Thio-COF was fabricated via the acid-catalyzed reaction of Tp with thioether substituted diamine, which was highly stable toward the water and common organic solvents (acetone, dichloromethane, ethanol, and tetrahydrofuran, etc.).<sup>92</sup> The introduction of the thioether group was beneficial for metal deposition and nanoparticle growth, paving the way for various applications, including optical and electronic devices.

In addition, Michael's addition-elimination strategy can also be used to construct  $\beta$ -ketoenamine linked COFs.<sup>93</sup> A series of COFs was fabricated in a one-step process via the reaction of aromatic amines with di- and tritopic ketoenols. The disappearance of the N-H and C-N stretching at  $3470$ ,  $3420$ , and  $1206\text{ cm}^{-1}$  together with the appearance of a new C-N band at  $1200\text{ cm}^{-1}$  in FT-IR spectra confirmed the formation of  $\beta$ -ketoenamine linkage. The obtained  $\beta$ -ketoenamine linked COFs exhibited improved hydrolytic stability owing to the intramolecular hydrogen bonding. The electron delocalization in these COFs generated a narrower band gap and reversible electrochemical doping. Moreover, a wide range of nucleophilic and electrophilic building units can be employed to form this kind of COFs.

#### 2.5. Hydrazone Linkage

Reversible condensation of hydrazides with aldehyde building unit yields a crystalline hydrazone-linked structure, which offers the

possibility of designing new linkages for COF synthesis. The first two hydrazone-linked COFs, COF-42 and COF-43, were reported in 2011, which were assembled via reversible dehydration of 2,5-diethoxyterephthalohydrazide and 1,3,5-triformylbenzene (TFB) or 1,3,5-tris(4-formylphenyl)benzene under solvothermal condition.<sup>94</sup> 2D trigonal layers were formed originating from the coplanar feature of hydrazone moiety and aromatic rings. The hydrazones remained the integrity even when COF-43 was submerged into solvents H<sub>2</sub>O, dioxane, and dimethyl formamide.<sup>95</sup> Moreover, the hydrazone-linked COFs have relatively weak interlayer interactions, such that they can be exfoliated into few-layer 2D polymers under mild conditions.

The high robustness and easy processible nature of hydrazone COFs make them popular in various applications.<sup>96,97</sup> The first visible-light-active COF was designed and prepared based on hydrazone linkage with the copolymerization of 2,5-diethoxyterephthalohydrazide and 1,3,5-tris-(4-formyl-phenyl)triazine (TFPT).<sup>35</sup> In the presence of Pt, the system produced 230–1970  $\mu\text{mol h}^{-1} \text{g}^{-1}$  of hydrogen. Later, a hydrazone-linked TFB-COF was constructed from TFB and 2,5-dimethoxyterephthalohydrazide with a BET surface area of 1501  $\text{m}^2 \text{g}^{-1}$ , which can be used as photocatalyst for cross-dehydrogenative coupling reactions.<sup>98</sup> Another two hydrazone COFs with rich hydroxy units were synthesized using water and then incorporated with Co<sup>II</sup> to investigate their Lewis acid catalytic activity.<sup>94</sup> As a result, the metallated COFs were effective in catalyzing the cyanosilylation reactions of various aldehydes.

## 2.6. Azine linkage

The first azine-linked COF was synthesized by the condensation of 1,3,5,8-tetrakis(4-formylphenyl)pyrene with hydrazine.<sup>99</sup> For azine linkage, hydrazine acted as a common building block to react with diverse aldehydes, which enables the formation of various functional COFs.<sup>100, 101</sup> For example, the visible-light-involved hydrogen generation from water can be achieved by the adjustment of COF structure. Three numbers of water- and photo-stable azine-based N<sub>x</sub>-COFs (x=0, 1, 2, 3, represent the number of nitrogen in central aryl ring) were synthesized by the polymerization of hydrazine and triphenylarene aldehydes.<sup>102</sup> Raman and FT-IR spectra were employed to confirm the presence of azine C=N linkage. As demonstrated, the photocatalytic hydrogen evolution was enhanced with the increased nitrogen content. Similarly, another series of azine-linked COFs with varied nitrogen atoms in the peripheral aryl ring was prepared for the investigation of photocatalytic hydrogen evolution.<sup>103</sup> The results suggested that even the very slight changes at the molecular level had a huge influence on the nanoscale morphology, atomic-scale structure, and optoelectronic properties, thereby causing significant differences in the capability of photocatalytic hydrogen production.

## 2.7. Imide-based linkage

In addition, a series of crystalline polyimide (PI) COFs, denoted as PI-COFs, was fabricated via reversible imidization reaction.<sup>104</sup> Simply by extending building molecules, the large pore size of as-prepared PI-COFs could be tuned. PI-COF-3 with a pore size of 5.3 nm and BET surface area of 2,346  $\text{m}^2 \text{g}^{-1}$  was designed and prepared by imidization condensation of 1,3,5-tris[4-amino(1,1-biphenyl-4-

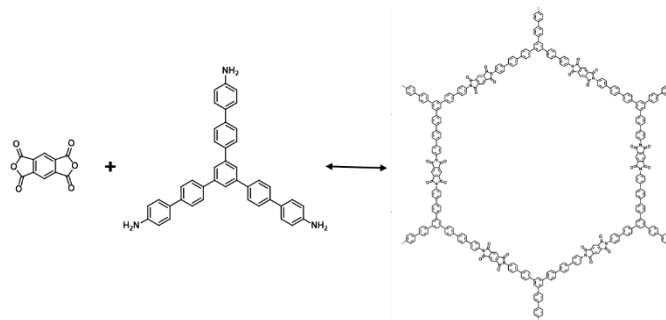


Fig. 5 The formation of PI-COF-3.

yl)]benzene (TABPB) with pyromellitic dianhydride (PMDA) in a mixed solvent of mesitylene, N-methyl-2-pyrrolidone (NMP), and isoquinoline (Fig. 5). The presence of C=O stretches at 1779 and 1718  $\text{cm}^{-1}$  and C-N-C stretching vibration at 1382  $\text{cm}^{-1}$  in FT-IR spectra revealed the formation of imide linkage in PI-COF-3. By linking the linear building unit PMDA and triangular building unit TABPB, PI-COF-3 was formed like a boron nitride net.<sup>105</sup> The material remained stable in water and common organic solutions, such as acetone, ethanol, m-cresol, N,N-dimethylformamide, tetrahydrofuran, and hexanes. Notably, the large dye molecules can also be incorporated into PI-COF-3 with distinctive applications. Other functional building blocks have been utilized in the formation of imide-based COFs, such as PMDA and 1,3,5,7-tetraaminoadamantane or tetra(4-aminophenyl)methane,<sup>106</sup> PMDA and tetramino-benzoquinone,<sup>107</sup> and pyromellitic carboxylic dianhydride and tetra(4-aminophenyl)porphyrin (TAPP).<sup>108</sup>

## 2.8. Other Linkages

Besides the above-mentioned linkages, other linkages have also been used in COF fabrication such as carbamate linkage,<sup>109</sup> borosilicate linkage,<sup>110</sup> phenazine linkage,<sup>111</sup> and squaraine linkage.<sup>112</sup> For example, a 3D borosilicate-linked COF was first synthesized by condensation of tetra(4-dihydroxyboryl-phenyl)methane, *tert*-butylsilane triol, and <sup>t</sup>BuSi(OH)<sub>3</sub>.<sup>110</sup> The as-prepared COF (named COF-202) possessed a BET surface area of 2690  $\text{m}^2 \text{g}^{-1}$  and high stability. Later, a crystalline borazine-linked COFs named BLP-2(H) was prepared by thermal decomposition of 1,3,5-(*p*-aminophenyl)-benzene-borane.<sup>113</sup> This as-prepared COF showed a BET surface area of 1178  $\text{m}^2 \text{g}^{-1}$ . A squaraine-linked COF with zigzagged confirmation was achieved by the copolymerization of copper(II) 5,10,15,20-tetrakis(4-aminophenyl)porphyrin (TAP-CuP) and squaric acid (SQ).<sup>112</sup> As indicated in FT-IR spectra, C=O bond (1595  $\text{cm}^{-1}$ ) was formed with a blue-shift compared with SQ (1579  $\text{cm}^{-1}$ ) due to the extended  $\pi$ -conjugation of the COF. This CuP-SQ COF with visible light absorption could act as an effective photocatalyst for singlet oxygen generation.

In addition, two crystalline benzobisoxazole-linked (BBO) COFs were prepared by the condensation of 2,5-diamino-1,4-benzenediol dihydrochloride with TFB or 1,3,5-tris(4-formylphenyl)benzene (TFPB) under the catalysis of cyanide.<sup>114</sup> A three-step mechanism was proposed to explain the BBO linkage formation: (1) a phenolic imine linked intermediate was first formed, (2) then ring closure took place with the addition of cyanide to the imine and a benzoxazoline

intermediate appeared, and finally (3) the benzoxazoline intermediate was oxidized under air, thereby promoting the BBO linkage formation.<sup>115</sup> The resulting BBO-COF 1 and BBQ-COF 2 displayed excellent water stability and the high surface area of 891 m<sup>2</sup> g<sup>-1</sup> and 1106 m<sup>2</sup> g<sup>-1</sup>, respectively. In another study, a room-temperature solution-phase reaction was employed to synthesize an azodioxy-linked COF (POR-COF) with I<sub>2</sub>-doping-enhanced photocurrent generation.<sup>116</sup> A series of spiroborate-linked ionic COFs (ICOFs) was synthesized with a high BET surface area up to 1259 m<sup>2</sup> g<sup>-1</sup>, constructed from the transesterification of diol and trimethyl borate.<sup>117</sup> Recently, the unsubstituted olefin-linked COF (COF-107) was first synthesized by Aldol condensation of 4,4'-biphenyldicarbaldehyde and 2,4,6-trimethyl-1,3,5-triazine (TMT) (Scheme 2).<sup>26</sup> FT-IR and <sup>13</sup>C CP-MAS spectroscopy were utilized to verify the formation of -CH=CH- linkage. The as-synthesized COF-701 possessed a BET surface area of 1715 m<sup>2</sup> g<sup>-1</sup> and high chemical robustness owing to the existence of unsubstituted olefin linkage.

As discussed above, various linkage motifs have been designed relating to the COF formation. Different linkages lead to different structures and properties, which usually correlated with the stability. It is easy to understand that the stability of COFs, especially in water and under light irradiation, is of crucial importance in their photocatalytic application. COFs based on boroxine and boronate ester linkages are susceptible to hydrolyze under the humid condition.<sup>118</sup> Though enhanced stability has been achieved by protecting electron-deficient boron centers from degradation, such as the ionic spiroborate-linked COF<sup>117</sup> and the alkylated COF-14Å,<sup>119</sup> their applications to photocatalysis have still been hindered and limited studies have been done. Different from boron-based COFs, imine-linked and other nitrogen-containing COFs are more robust. Interlayer complementary  $\pi$ -interactions and intralayer hydrogen-bonding interactions have been developed to improve the stability of imine-linked COFs.<sup>120, 121</sup> Similarly,  $\beta$ -ketoenamines-linked COFs originating from the enol-keto tautomerization of their imine counterparts show a much higher stability, and have been used in photocatalysis.<sup>87, 122</sup> TzDTz COF (TpDTz: Tp and 4'-(thiazolo[5,4-d]thiazole-2,5-diyl)dianiline) was stable in boiling water and strongly acid for up to 7 days, and the morphology, structure, crystallinity were retained after a 72 h long photocatalysis experiment.<sup>123</sup> COFs with hydrazone and azine linkages are also active in photocatalytic process.<sup>124-126</sup> The studies revealed that COFs obtained after photocatalysis retained the connectivity and photoactivity, although losing a part of long-range order which could be ascribed to the exfoliation in water and can be recovered in the original reaction conditions. Compared to the imine, hydrazine and azine COFs, triazine and phenazine-linked COFs show exceptional chemical stability, and triazine unit as a photoactive group have been widely explored in photocatalysis.<sup>127-129</sup> As for the newly developed C=C-linked sp<sup>2</sup> COF, extremely high stability has been found in the photocatalytic experiment. Under the light irradiation of 16 h, while imine-linked COF-LZU1 nearly lost its crystallinity in 4 h, g-C<sub>18</sub>N<sub>3</sub>-COF with C=C linkages exhibited retained structure and activity despite a slight decay of crystallinity.<sup>130</sup> Remarkably, the excellent photostability of g-C<sub>40</sub>N<sub>3</sub> was proved by the nearly constant

photocurrent density within the measurement period of 2600 s.<sup>131</sup> Unlike MOFs, most COFs show enhanced stability because of the covalent bond, but it is still the key point to improve the water- and photostability of COF photocatalysts for practical application.

### 3. Morphology of COFs

One of the most common design strategies for optimizing photocatalytic performance is morphology control. Abundant building blocks and functional covalent linkages endow COFs with a designable structure. Indeed, many studies have been done to investigate the features of COFs with special structures, including 0D nanoparticles,<sup>117, 132</sup> 1D nanofibers, nanowires and nanorods,<sup>133, 134</sup> 2D thin films and nanosheets,<sup>135, 136</sup> and 3D hollow structure.<sup>137, 138</sup> The morphology and structure investigations of COFs are of great importance for their photocatalytic performance. In this section, the synthesis and photocatalytic properties of COFs on the morphologies were discussed.

#### 3.1. 0-dimensional nanoparticles

0D-structural materials are considered as promising photocatalysts due to the large surface area.<sup>139</sup> However, their photocatalytic performance still suffers from low efficiency due to the large agglomeration. In most cases, the monomers of COF are partially soluble in reaction solvents, leading to a heterogeneous growth condition, thereby making it hard to understand the crystallization process. Currently, most of the reported COFs are synthesized with poor controlled morphology and form insoluble and unprocessable aggregates. Recently, a strategy of homogeneous polymerization was put forward to avoid the irreversible aggregation and precipitation of crystallites, providing stable colloidal suspensions of COF nanoparticles.<sup>139</sup> By adding a certain amount of CH<sub>3</sub>CN in a conventional solvothermal mixture of COF-5, translucent solution with nanoparticles was obtained. CH<sub>3</sub>CN was demonstrated to stabilize the discrete crystallites and inhibit their aggregation in solution (Fig. 6a and 6b). Further investigation demonstrated that the interaction of the COF and nitrile functional group was responsible for the nanoparticle formation. Interestingly, the real-time growth of individual nanoparticles was observed using variable-temperature liquid cell transmission electron microscopy (VT-LCTEM) imaging (Fig. 6c). These stable porous nanoparticles with the functional internal surface were capable of site-isolated catalysis. Besides, a two-step approach was utilized to further control the formation of 2D COFs, which provided single-crystalline and micrometer-sized particles.<sup>140</sup> When heating the COF-5 colloidal suspension, separated solutions of HHTP and PBBA were simultaneously injected, generating COF-5 nanoparticles with the sizes of 30-400 nm. To verify the generality of this strategy, the other two boronate ester-linked COF-10 and TP-COF were also studied. And later, the research was further expanded to the imine-linked COF. Colloidal TAPB-PDA COF nanoparticles were obtained by adding MeCN in the reaction system, which possessed a high BET surface



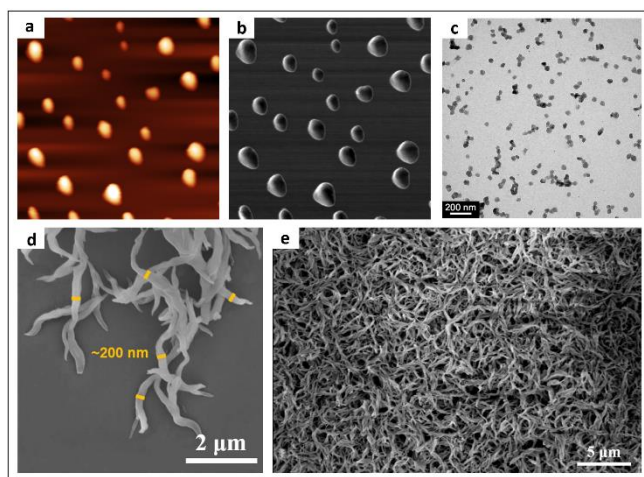


Fig. 6 (a, b) AFM of COF colloids prepared at 75% solvent concentration of  $\text{CH}_3\text{CN}$ . (c) Representative VT-LCTEM image of COF-5 nanoparticles (55% growth solution). Reproduced with permission from ref. 139. Copyright 2017, American Chemical Society. (d) SEM images of  $\text{g-C}_{18}\text{N}_3\text{-COF}$ . (e) Top view SEM micrograph of  $\text{g-C}_{18}\text{N}_3\text{-COF}$  film. Reproduced with permission from ref. 130. Copyright 2019, American Chemical Society.

area of  $2070 \text{ m}^2 \text{ g}^{-1}$ .<sup>141</sup> Similarly, considering the narrow range of nanoparticle size, separated solutions of TAPB and PDA were injected simultaneously to TAPB–PDA COF colloids solution. And the morphologies of the particles varied with the different monomer addition rates.

Nanoparticles with favorable surface speciation are deemed to display excellent photocatalytic activity compared with their bulk-phase counterparts. In addition, by reducing the particle size, the CB and VB could be shifted to counterparts considering the quantum confinement effect, thus improving the redox potential of photogenerated electrons and holes.<sup>12, 142</sup> However, the study of COF photocatalysts with OD structure remains challenging.

### 3.2. 1-dimensional structures

With high surface-to-volume ratio, the research of 1D structures such as nanofibers, nanoribbons, and nanowires have increased over the years.<sup>143</sup> The study of COF morphology related to 1D structures is of great value. Up to date, solvothermal synthesis,<sup>144</sup> vapor-assisted solid-state synthesis,<sup>145</sup> and bottom-up microfluidic synthesis<sup>146</sup> have been used to fabricate crystalline COF fibers. For example, novel crystalline COF nanofibers were fabricated by the solvothermal method based on the co-polymerization of 2,4,6-tris(4-aminophenyl)-pyridine (TAPP) with 2,6-Dihydroxynaphthalene-1,5-dicarbaldehyde (DHNDA) at  $180^\circ\text{C}$ .<sup>144</sup> The as-prepared COF was formed as uniform nanofibers with lengths of up to tens of micrometers. Interestingly, it was indicated the morphology transformed from irregular nanoparticles to uniform nanofibers with increased crystallinity, which may be ascribed to the dissolution-recrystallization process. This transformation enabled the fabrication of COF nanohybrid with excellent optical and electrical properties. Similarly, nanofibers could also be obtained via vapor-assisted solid-state synthesis.<sup>145</sup> Different from the solvothermal synthesis, the polycondensation of TAPP and DHNDA was carried out by putting the mixture of monomers in solvent vapor at  $120^\circ\text{C}$  for 48 h. In this method, only a small quantity of solvent vapors was needed, and the

nanofibrous morphology was varied with the reaction time and the solvent vapor composition.

Likewise,  $\text{g-C}_{18}\text{N}_3\text{-COF}$  with fibrillar morphology was prepared by Knoevenagel condensation of 1,4-diformylbenzene (DFB) with 2,4,6-trimethyl-1,3,5-triazine (TMTA) (Fig. 6d and 6e).<sup>130</sup> The ultraviolet-visible diffuse reflectance spectroscopy (UV-vis DRS) displayed that the absorption band edge of  $\text{g-C}_{18}\text{N}_3\text{-COF}$  was at 450 nm, indicating a strong visible-light harvesting. And  $\pi$ -conjugated  $\text{g-C}_{18}\text{N}_3\text{-COF}$  with an average lifetime of 7.25 ns revealed the suppressed photogenerated electron-hole recombination. With ascorbic acid as a sacrificial agent and Pt as a co-catalyst, an average  $\text{H}_2$  production rate of  $292 \mu\text{mol g}^{-1} \text{ h}^{-1}$  was achieved over  $\text{g-C}_{18}\text{N}_3\text{-COF}$ . In addition, COFs bearing Tp and melamine (MA) building units with visible-light-response features were synthesized as exfoliated thin ribbon-like and interwoven thread-shaped structures under different conditions (catalyst-assisted, solvent-assisted, and liquid-free) by ball milling.<sup>134</sup> Compared to the thread-shaped COF, the optical absorption edge of ribbon-like COF displayed a red-shift, enhancing solar utilization efficiency, and therefore leading to a higher photocatalytic degradation rate of phenol. These findings suggested that the morphology affected the photocatalytic activity of COF-based materials, which may be ascribed to the aggregation behavior, dispersity, and incident light-harvesting capability in water.

### 3.3. 2-dimensional thin films and nanosheets

The optical, photochemical and photoelectrical features of the materials could be affected directly or indirectly if their morphology and structure are changed. In addition to the OD and 1D structures, 2D structures like thin films and few-layered nanosheets have also been widely studied in the photocatalytic process.<sup>147, 148</sup> Indeed, the high smoothness and aspect ratio along with the short travel distance of the photoexcited carriers render the thin films with high photocatalytic performance.<sup>149, 150</sup> In recent years, various methods have been utilized to synthesize COF thin films as free-standing forms or deposited on specific substrates, such as mechanical delamination,<sup>88, 151</sup> solvent-assisted exfoliation,<sup>152, 153</sup> solvothermal synthesis<sup>154, 155</sup> and interfacial synthesis.<sup>156, 157</sup> Among them, solvothermal synthesis is widely used because it is simple and straightforward. For example, TT-COF thin films with a 200 nm thickness were prepared on the cleaned glass substrate by simply immersing the substrate in the solution of bulk TT-COF synthesis.<sup>158</sup> As demonstrated by grazing incidence X-ray diffraction (GIXRD), the growth of 2D TT-COF thin films was parallel to the surface of the glass substrate, which indicated an ordered charge transfer pathway. Greatly enhanced photoresponse speed was observed in the well-ordered COF thin film.

In another study, BDT-ETTA COF based on amine-functionalized 1,1',2,2'-tetra-*p*-aminophenylethylene (ETTA) and donor-type benzo[1,2-*b*:4,5-*b'*]-dithiophene-2,6-dicarboxaldehyde (BDT) was grown on indium tin oxide substrate to yield BDT-ETTA COF thin films.<sup>159</sup> The obtained COF thin films displayed strong visible light absorption with a threshold of *ca.* 550 nm and a band gap of 2.47 eV, indicating a photoactive potential. The results suggested that the BDT component could be the reason for the photoactivity, and the oriented COF thin films as the precondition amplified the



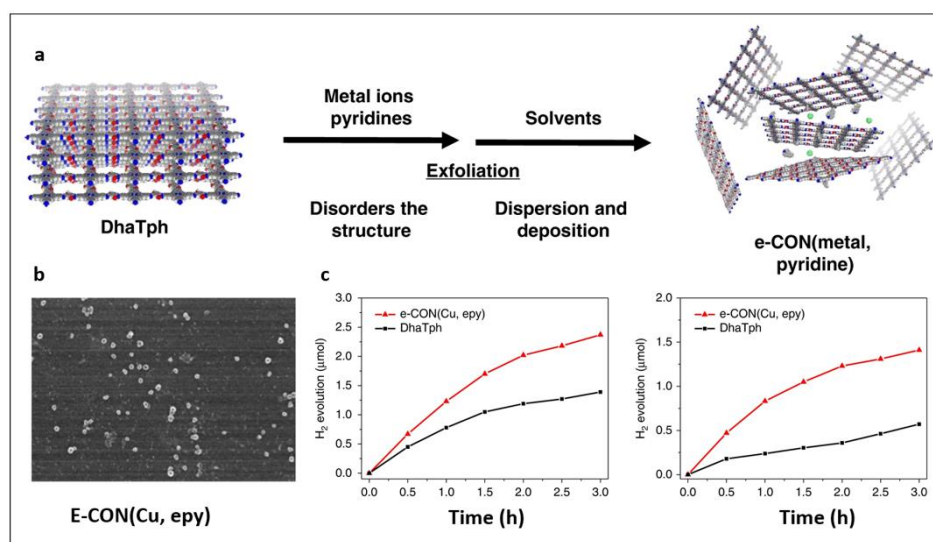


Fig. 7 (a) Scheme for the formation of e-CON. (b) SEM image of e-CON (Cu, epy) deposited on the silicon wafer. (c) H<sub>2</sub> evolution upon irradiation with visible (>420 nm) and NIR (>780 nm) light using e-CON(Cu, epy)/Pt/RGO and DhaTph /Pt/RGO. Reproduced with permission from ref. 161. Copyright 2019 Springer Nature Limited.

photoresponse and improved the stability. A new synthetic method was employed by directly condensing 3,4,9,10-perylene-tetracarboxylic diimide (PDI) and cyanuric chloride (CC) to yield a CTF film photocatalyst.<sup>160</sup> CTF film with excellent photocatalytic activity showed an enhanced NADH regeneration of 75.88 % and HCOOH production of 204.14 μmol. Also, ultrathin 2D porphyrin nanodisks with enhanced photocatalytic activity were prepared by COF exfoliation via axial ligands incorporation. Porphyrin-containing COF DhaTph (Dha: 2,5-dihydroxyterephthalaldehyde, Tph: 5,10,15,20-tetrakis(4-aminophenyl)-21H,23H-porphyrin) was exfoliated by simultaneously incorporating 4-ethylpyridine and copper (Cu) ions ligands into the porphyrin center to yield e-CON(Cu, epy) (Fig. 4a and 4b).<sup>161</sup> The resulting e-CON was further incorporated with Pt nanoparticles and reduced-graphene oxide (RGO) to obtain composite materials e-CON(Cu, epy)/Pt/RGO for photocatalytic reaction (Fig. 4c). Compared with DhaTph/Pt/RGO, an enhanced visible/NIR-light-induced hydrogen evolution of e-CON(Cu, epy)/Pt/RGO system was observed owing to the higher surface area between e-CON and Pt/RGO. The abovementioned results demonstrated that the 2-dimensional COF thin films and nanosheets with broad light absorption, optical band gap, and efficient charge separation and transfer have great potential for photocatalytic activity improvement.

### 3.4. 3-dimensional hollow structures

COFs with 3D structures are synthesized mainly by heterogeneous nucleation growth,<sup>162, 163</sup> template-directed approach,<sup>137, 164, 165</sup> self-assembly strategy,<sup>163, 166, 167</sup> multiple-linking-site strategies.<sup>168</sup> In the study of Zhao and co-workers, methyl groups were introduced into triptycene tricatechol (TPTC) to increase the space between monolayers, thus further weaken the  $\pi$ - $\pi$  stacking interactions.<sup>169</sup> As a result, the floating film-like structure was obtained by solvothermal condensation of TPTC and BDBA or 4, 4'-biphenyldiboronic acid (BPDBA), respectively. Interestingly, mono-layered and multi-layered hollow spherical structures were found to exist. Different from

stacking structures obtained from conventional solvothermal reactions, the condensation of TPTC with boronic acids first produced single-molecule-layered 2D frameworks. As the polymerization time progressed, the monolayers occurred curly and tended to form mono-layered hollow spheres driving by surface energy reduction. And the layers would also enwrap the mono-layered spheres to generate uniform multi-layered hollow microspheres. While the abovementioned hollow spherical COF showed poor crystallinity, a crystalline hollow spherical COF, namely DhaTab, was synthesized based on 1,3,5-tris(4-aminophenyl)benzene and 2,5-dihydroxyterephthalaldehyde by self-template synthesis.<sup>166</sup> Two steps were involved in constructing the hollow spherical structure: first, COF-DhaTab with rod-like morphology was first formed within 12 h, and then randomly self-assembled into curly or dense spheres (Fig. 8a). An inside-out Ostwald ripening was invoked in the formation of hollow spherical morphology for the next 24 h as the crystallites in inner sphere got higher surface energy than those on the outer surface, and crystallites on the sphere wall fused to produce a smooth surface with the time increased (Fig. 8b and 8c).

In addition, a template-assisted synthesis method has also been used in constructing hollow nanostructures. For example, Hollow TpPa COF was designed and synthesized with the assist of ZnO nanorod template.<sup>137</sup> First, *p*-phenylenediamine (Pa) and Tp were dehydrated in the presence of ZnO nanorods, and then the ZnO nanorods were removed by treating the produced hybrid materials with acid (1N HCl) for 24 h, leading to the formation of hollow TpPa nanostructures with the inner and outer diameters of  $d = (70-130)$  nm and  $d = (60-100)$  nm, respectively. Another imine-linked TpBD COF containing Tp and benzidine (BD) building blocks were directly grown on Fe<sub>3</sub>O<sub>4</sub> by a solvothermal method to form a core-shell structural TpBD@Fe<sub>3</sub>O<sub>4</sub>.<sup>163</sup> The hollow TpBD was further obtained by etching the Fe<sub>3</sub>O<sub>4</sub> core in HCl solution, resulting in a shell thickness of *ca.* 50 nm. These references could offer an important process for

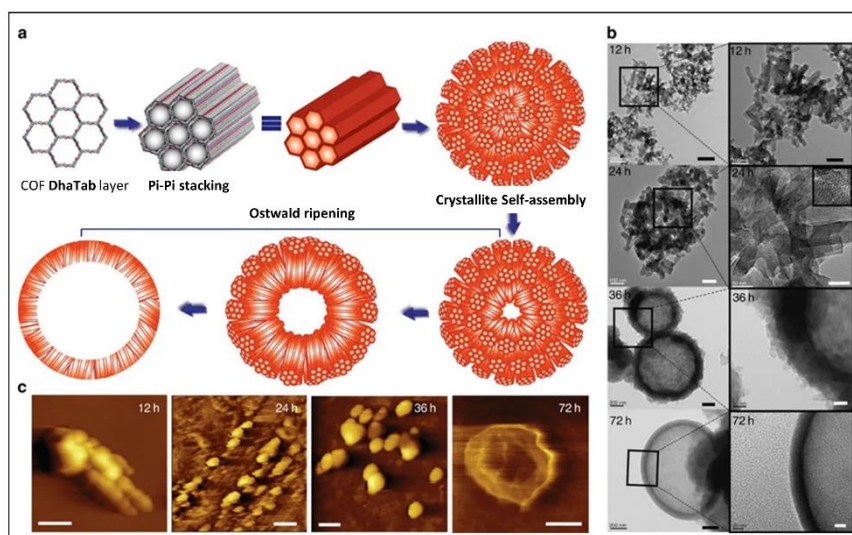


Fig. 8 (a) Scheme illustration of COF hollow sphere formation. (b, c) TEM and AFM images of COF-DhaTab, respectively, recorded at different intervals of time. Reproduced with permission from ref. 175. Copyright 2015 Macmillan Publishers Limited.

the construction of COF-based photocatalysts. The hollow structures obtained from a template-assisted method possess ordered and uniform cavities simply by controlling the template diameter. Hollow structure with controlled porosity reduces diffusion length and improves contact of active sites with reactants.<sup>170, 171</sup> Moreover, the multiple reflections within the hollow cavity are benefit for the efficient light utilization, producing more photogenerated charge carriers.<sup>172, 173</sup>

#### 4. Strategies for enhancing the photocatalytic activity of COFs

Based on the typical photocatalytic process, the design and modification of photocatalysts with enhanced performance would involve considerations such as extended visible-light-absorbing capacity, facilitated electron-hole separation and suppressed photocorrosion for prolonged duration. COFs as a flexible platform show promising applications in photocatalysis and several strategies have been developed for enhancing their activity based on pristine COFs and modified COFs. To increase the visible-light adsorption and decrease the recombination of photogenerated electrons and holes, the most direct way lies in the elaborate incorporation of functional building blocks to modulate the optical and electrical features of COFs. The physical and chemical properties of COFs can be changed by the selection of building blocks, which enables the control of their band gap structure at molecular level. In addition, elemental doping including nonmetal doping and metal doping can also be a facile and feasible strategy to tune the physicochemical properties of COFs at atomic level. Band gap engineering can be realized by introducing anions and cations into the framework for improving the light-harvesting capability and tuning redox band potentials. Effectively utilizing solar energy in a large span of spectrum is critical for photocatalytic process. To further broaden the light absorption to a higher wavelength range, the incorporation of sensitizer is another

fascinating strategy to enhance the photocatalytic activity. Photosensitizers with chromophore are expected to extend the light absorption to NIR region and the well-matched band gap structures of COFs and sensitizers also could accelerate the charge separation at their interfaces. Besides, COFs with diverse functional groups and -stacking nanosheets act as an ideal platform for the fabrication of hybrid materials with various semiconductors. The formation of COF-based hybrid photocatalysts is deemed to be a feasible and compelling strategy for photocatalytic activity improvement, which owns advantages of enlarging visible-light adsorption, facilitating the electron transfer between composites, and enhancing separation efficiency of photogenerated electron-hole pairs.

##### 4.1. Functional building blocks incorporation

One of the most attractive characteristics of COFs related to photocatalysis is their regular structures with unlimited building blocks, which can be applied to various reaction conditions. Based on reticular chemistry, COFs allow a predesigned pathway for precise controlling over their structures and properties by choosing different linkers as well as different building units containing function groups or side chains.<sup>108, 174-178</sup> Up to date, functional building blocks incorporation is the most widely used strategy for modulating the photocatalytic performance of COFs. For example, a series of azine-linked  $N_x$ -COF photocatalysts were synthesized by selecting hydrazine as the linker and triphenylarene aldehydes as the nodes, in which the nitrogen atoms of central aryl ring in aldehyde units varied from 0 to 3 (Fig. 9a and 9b).<sup>102</sup> Replacing the carbon atoms with nitrogen atoms led to the formation of different central rings namely phenyl ( $N = 0$ ), pyridyl ( $N = 1$ ), pyrimidyl ( $N = 2$ ), and triazine ( $N = 3$ ), showing the increased planarity due to the decreased dihedral angle between peripheral phenyl rings and the central aryl ring. Consequently, increased crystallinity was observed as a result of the increasing nitrogen contents (Fig. 9c). It was found that the increased crystallinity and improved structural definition and layer registry endowed  $N_3$ -COF with enhanced exciton migration in-plane

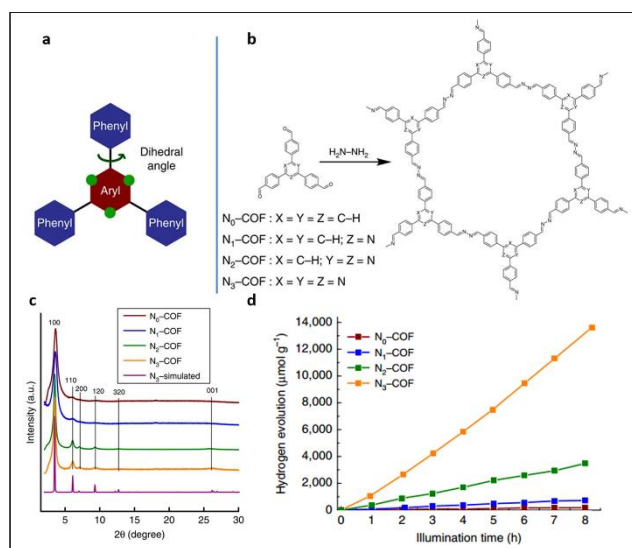


Fig. 9 (a) A tunable triphenylarene structure. (b) Formation of  $N_x$ -COFs based on hydrazine and  $N_x$ -aldehydes. (c) PXRD patterns of the  $N_x$ -COFs compared with the simulated pattern calculated for the representative  $N_3$ -COF. (d)  $H_2$  production monitored over 8 h using  $N_x$ -COFs as photocatalyst in the presence of triethanolamine as a sacrificial electron donor. Reproduced with permission from ref. 102. Copyright 2015 Macmillan Publishers Limited.

as well as along the stacking conjugation, thus leading to the improved photocatalytic activity (Fig. 9d). In addition,  $N_3$ -COF as the most nitrogen-rich COFs in the system showed an increased stabilization of radical anions which determined to enhance the charge separation and electron migration. Besides,  $\pi$ -conjugated *trans*-disubstituted C=C linked COFs (termed  $g-C_xN_y$ -COFs) with different properties were designed and synthesized based on the Knoevenagel condensation of 3,5-dicyano-2,4,6-trimethylpyridine (DCTMP) with linear 4,4'-diformyl-*p*-terphenyl (DFTP), 4,4'-diformyl-1,1'-biphenyl (DFBP), or TFPB, which yielded  $g-C_{40}N_3$ -COF,  $g-C_{31}N_3$ -COF, and  $g-C_{37}N_3$ -COF, respectively.<sup>179</sup> As demonstrated by UV-vis DRS,  $g-C_{40}N_3$ -COF showed a significant red-shift of absorption edge compared with  $g-C_{31}N_3$ -COF and  $g-C_{37}N_3$ -COF, indicating a stronger ability of light-harvesting in the visible region; and  $g-C_{40}N_3$ -COF with a smaller optical band gap (2.35 eV) was observed as compared to  $g-C_{31}N_3$ -COF (2.40 eV) and  $g-C_{37}N_3$ -COF (2.52 eV). Time-resolved fluorescence decay spectroscopy was also used to characterize the excitation recombination with the information of the average lifetime of photo-excited electrons. As a result,  $g-C_{40}N_3$ -COF exhibited the most extended fluorescence lifetime (3.31 ns) due to the charge separation in the extended  $\pi$ -conjugated structure. These findings along with other optical and electronic characterizations (Mott-Schottky measurement, photocurrent tests, etc.) suggested that  $g-C_{40}N_3$ -COF permitted the effective photogenerated electron-hole transfer, and thereby the enhanced photocatalytic ability. These examples demonstrated that the photocatalytic performance of COFs can be enhanced by precisely selecting of building units.

Various functional building blocks such as triazine,<sup>180</sup> sulfone,<sup>124</sup> pyrene,<sup>181</sup> benzothiadiazole,<sup>182</sup> and thiophene,<sup>183</sup> have been utilized for constructing COF photocatalyst with high performance. For

example, diacetylene-bridged COFs were of great interest owing to the highly conjugated structures, accessible active sites, and accelerated charge transfer.<sup>184</sup> Porous and stable acetylene ( $-C\equiv C-$ ) and diacetylene ( $-C\equiv C-C\equiv C-$ ) functionalized  $\beta$ -ketoenamine COFs, TP-EDDA and TP-BDDA, were prepared and their photocatalytic properties were carried out (Fig. 7).<sup>91</sup> Ketoenamine linkage was introduced to ensure the chemical stability of the COFs. To well-determine the influence of acetylene and diacetylene functional groups, an isorecticular COF TP-DTP COF (DTP: 4,4'-diamino-*p*-terphenyl) with similar pore apertures based on terphenylene edges was designed and prepared. Determined by UV-vis spectra, TP-BDDA showed an absorbance edge of 525 nm and the tail extended up to 675 nm, while the absorbance edge of TP-EDDA and TP-DTP was 520 nm and 500 nm, respectively. Similarly, the optical band gaps followed the order of TP-BDDA (2.31 eV) < TP-EDDA (2.34 eV) < TP-DTP (2.42 eV). Photocatalytic experiments indicated that the conjugated diacetylene group played a vital role in enhancing the photoactivity. Apart from narrowing the band gap, diacetylene-moieties were also considered to possess higher charge carrier mobility and enable the accelerated migration of photogenerated excitons to the surface of photocatalyst. In addition, electron acceptor such as benzothiadiazole (BT), and electron donors such as tris-(4-aminophenyl)triazine (TAPT) and tris(4-aminophenyl)benzene (TPB) were employed to construct COFs with tailored band gaps and improved charge separation and transfer.<sup>182</sup> The resultant BT-COFs showed the extended absorption bands ranging from 400 nm to 800 nm. Compared to TAPT-BT-COF, TPB-BT-COF with narrower band gap and more negative conduction band was found to exhibit promoted visible-light harvesting efficiency and produce more charge carriers. And the photocurrent intensity and electrochemical impedance spectra further confirmed that the structure of TPB-BT-COF was beneficial for enhanced charge carrier separation and reduced charge transfer impedance.

#### 4.2. Elemental doping

Elemental doping is another efficient strategy to regulate the surface property and electronic structure of semiconductors, thereby improving the photocatalytic activity. The element sulfur (S), as one of the most common dopants, is known to modulate the electronic structure as well as the optical adsorption features of organic semiconductor photocatalysts.<sup>185, 186</sup> A series of S-doped CTFs were prepared by the annealing treatment of covalent triazine-based framework CTF-T1 with S, which were named as CTFs<sub>x</sub> ( $x = 5, 10, 20, 30$ ).<sup>129</sup> In this case, compared with the  $g-C_3N_4$  photocatalyst, CTFs<sub>x</sub> exhibited much better photocatalytic activity, and the CTFs<sub>10</sub> with the highest photoactivity was about 5 times higher than CTF-T1. Similarly, other typical non-metal dopants such as Halogens have also been utilized for photocatalysis improvement. A series of halogen (F, Cl and Br)-doped CTFs was synthesized via the thermal treatment of CTF-1 with excessive ammonium halide.<sup>187</sup> Halogen-doped CTF-1 with decreased Nyquist plot diameter and higher photocurrent density revealed the improved efficiency of charge separation and transfer as compared with pristine CTF-1 (Fig. 10a and 10b). The optical band gap of CTF-1, CTF<sub>F</sub>, CTF<sub>Cl</sub> and CTF<sub>Br</sub> was determined to be 2.94, 2.82, 2.48 and 2.63 eV (Fig. 10d). The



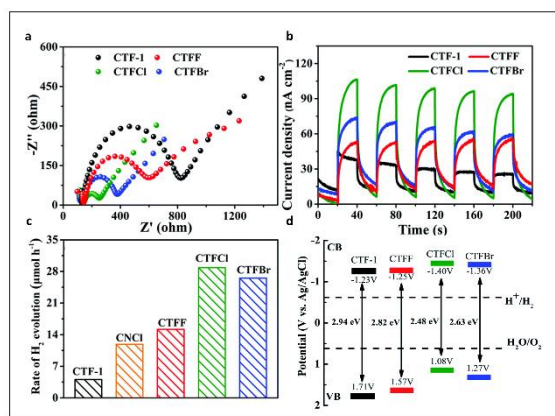


Fig. 10 (a) Electrochemical impedance spectroscopy plots of CTF-1 and CTF samples. (b) Photocurrent responses under visible-light irradiation of CTF-1 and CTF samples. (c) H<sub>2</sub> evolution rates of CTF-1, CTF and CTF samples. (d) The recycling performance of CTF for hydrogen evolution in five repeats. Reproduced with permission from ref. 187. Copyright 2016, Royal Society of Chemistry.

narrower band gaps and facilitated electron transfer in the modified  $\pi$ -conjugated CTF greatly enhanced the photocatalytic performance evidenced by 7.1 times higher photocatalytic ability of CTFCl compared to pristine CTF-1 (Fig. 10c).

In addition to the abovementioned non-metal doping, metals such as Fe, Zn, Re also have been doped into COFs for the modulation of their optical and electrical properties by narrowing the band gap, extending visible-light absorption, facilitating electron charge transfer, and increasing lifetime of charge carriers.<sup>188–190</sup> The nitrogen pots in the COFs provide rich binding sites for the incorporation of metal ions via an ion coordination. The inclusion of Re into CTF-py (based on 2,6-dicyanopyridine) was developed by Cao et al. for the first time.<sup>188</sup> Compared with CTF-py, Re-modified Re-CTF-py showed a lower charge transfer resistance, and a higher charge carrier separation efficiency. By incorporating Re into CTF-py, photogenerated electrons could transfer from CTF-py to Re and the recombination of electron-hole pairs was retarded, thus leading to the enhanced photocatalytic activity. Furthermore, BpZn-COP was synthesized by the coordination of Zn<sup>2+</sup> with N atoms of pyridine units in Bp-COF.<sup>190</sup> It was found that BpZn-COP showed a broader light adsorption (from 550 nm to more than 600 nm) and a narrower band gap (from 2.35 eV to 2.18 eV) compared to that of Bp-COP. The presence of Zn<sup>2+</sup> played an important role in promoting the electron transfer inside the bulk and across the interface of semiconductor and electrolyte, suppressing electron-hole recombination and improving the utilization efficiency of charge carriers. By this way, BpZn-COP displayed a much higher photocatalytic activity.

#### 4.3. Sensitizer

Light-harvesting is one of the most important prerequisites for electron-hole generation, which greatly affects the photocatalytic performance. Photosensitizer with intense visible light absorption can be used as a co-catalyst to enhance light absorption and the lifetime of photoinduced electron-hole pairs, thus improving the photocatalytic performance.<sup>191, 192</sup> The photocatalytic activity of COFs modified with palladium acetate was investigated by using

Eosin Y (EY) as a sensitizer.<sup>193</sup> Isorecticular COF-LZU1 and TpPa-1 were employed to facilitate energy transfer. As demonstrated, while Pd<sup>0</sup>/COF-LZU1 and Pd<sup>0</sup>/TpPa-1 were not photoactive without EY, they exhibited enhanced photocatalytic activity with the help of EY. When EY adsorbed visible light, electrons were generated and then transferred from COFs to Pd active sites for photocatalytic reaction. Furthermore, 2D COFs with  $\pi$ -conjugated structures could effectively facilitate the photogenerated electrons transfer, leading to the improved performance.

#### 4.4. Hybrid construction

In addition, hybrid materials with synergistic effects are believed to provide versatile characters for photocatalysis. By carefully design, multicomponent heterojunction materials with improved photocatalytic efficiency could be achieved regarding the promoted charge separation and enhanced charge carrier transfer. COFs-based composites have also been reported to show enhanced photocatalytic activity.<sup>161, 180</sup> Crystalline COF can serve as an attractive support matrix for nanoparticle loading due to its remarkable stability, high porosity and surface area.<sup>194</sup> Highly stable TpPa-2 COF was employed to anchor CdS nanoparticles.<sup>195</sup> The  $\pi$ -conjugated COF support was believed to enhance the photostability of the loaded CdS nanoparticles and suppress the photogenerated electron-hole recombination, thus enhancing the photocatalytic performance. After combination, a yellow to reddish brown shift was observed in the absorption spectra, which indicated an enhanced visible-light absorption of CdS-COF composite. And charge carriers transfer existed between CdS and COF, leading to the decreased photogenerated electron-hole recombination. As a result, an improved photocatalytic activity was achieved as compared to bulk CdS. Likewise, CdS nanoparticle-decorated CTF-1 (CdS NPs/CTF-1) was synthesized by an one-pot solvothermal reaction.<sup>196</sup> Size-controlled CdS NPs uniformly dispersed on CTF-1 layers surface with the interaction of Lewis basic nitrogen atoms in triazine groups of CTF-1. This interaction between CdS and CTF-1 endowed CdS with high stability and nanosized structure, and simultaneously promoted the photoinduced charge separation. A higher photocatalytic capability was realized by this CdS NPs/CTF-1 hybrid than pure CTF-1 and CdS under visible-light illumination. In addition, 2D layered BiOBr is frequently used in photocatalytic environment remediation and energy conversion because of its excellent electrical, optical, and catalytic features.<sup>197, 198</sup> However, its small surface area, poor light absorption, and high photoinduced electron-hole recombination limit the development. Hence, heterojunction based on CTFs and BiOBr could be developed to enhance photocatalytic activity.<sup>199</sup> It was revealed that BiOBr/CTF-3D-2% possessed much higher photocatalytic performance of tetracycline hydrochloride (TC-H) and ciprofloxacin (CIP) compared to pure BiOBr and CTF-3D.

Similarly, a novel MOF@COF core-shell hybrid material was constructed to possess high photocatalytic performance.<sup>200</sup> By virtue of its available amino functional groups and high stability under harsh experiment conditions, NH<sub>2</sub>-MIL-68 with 2-aminoterephthalic acid ligands and InO<sub>4</sub>(OH)<sub>2</sub> infinite chains were selected. As depicted in the scheme, NH<sub>2</sub>-MIL-68 was first synthesized through solvothermal reaction, and then functionalized by tris(4-formylphenyl)amine



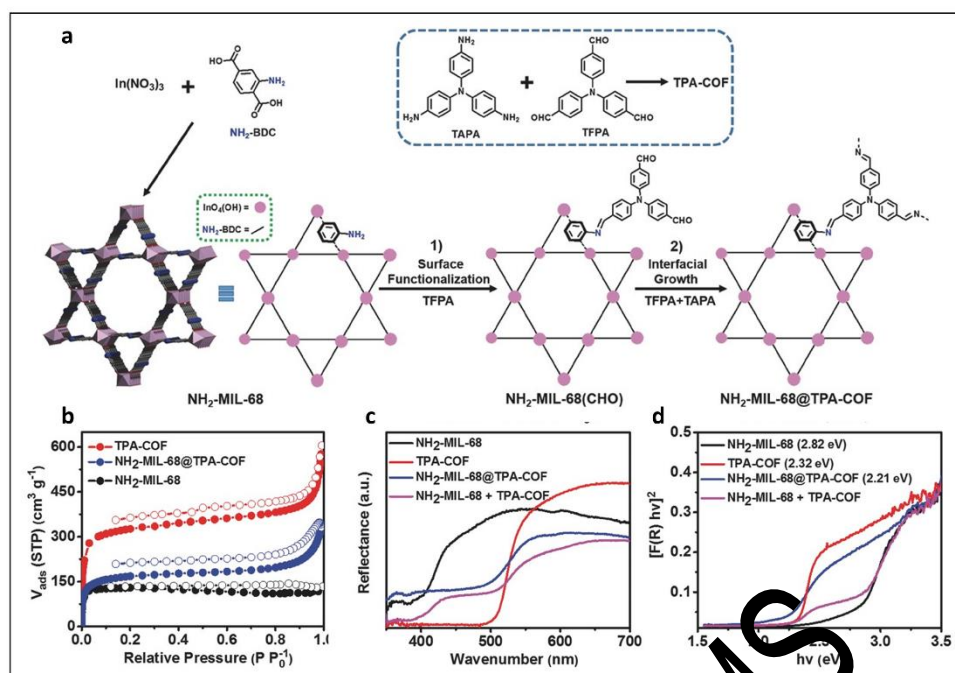


Fig. 11 (a) Schematic illustration of NH<sub>2</sub>-MIL-68@TPA-COF hybrid material synthesis. (b) N<sub>2</sub> sorption isotherms for NH<sub>2</sub>-MIL-68, TPA-COF, and NH<sub>2</sub>-MIL-68@TPA-COF measured at 77 K. (c) UV-vis DRS spectra, and (d) the plots of Kubelka-Munk function of NH<sub>2</sub>-MIL-68, TPA-COF, NH<sub>2</sub>-MIL-68@TPA-COF, and the mixture of NH<sub>2</sub>-MIL-68 and TPA-COF (NH<sub>2</sub>-MIL-68 + TPA-COF). Reproduced with permission from ref. 200. Copyright 2018, Wiley-VCH.

(TFPA) molecule to obtain aldehyde-functionalized NH<sub>2</sub>-MIL-68, donated as NH<sub>2</sub>-MIL-68(CHO). And TPA-COF was grown on NH<sub>2</sub>-MIL-68(CHO) surface by covalent linking tris(4-aminophenyl)amine with TFPA via conventional solvothermal condensation, generating core-shell structural hybrid NH<sub>2</sub>-MIL-68@TPA-COF (Fig. 11). NH<sub>2</sub>-MIL-68@TPA-COF displayed higher photocatalytic activity, which was about 1.4 times higher than that of NH<sub>2</sub>-MIL-68, due to its large surface area as well as smaller band gap.

As discussed above, strategies including functional building blocks incorporation, elemental doping, co-synthesis, and hybrid construction have been utilized in enhancing photocatalytic performance of COFs. Among them, while functional building blocks incorporation as the distinctive feature of COFs have been widely used, the exploration is far enough in view of the unlimited building molecules, and much work still needs to be done for the synthesis of new functional COFs. And post-synthetic modification will also be a promising strategy to utilize photoactive groups which are difficult for *ab initio* construction. Besides, heterojunction constructing attracts considerable interest. By building suitable band positions, it is able to transfer photogenerated electron-hole pairs from the interface to the surface of two components, which leads to redox and reduction reactions. Indeed, new strategies with high performance are highly desired.

## 5. Photocatalytic applications

### 5.1. Application in photocatalytic hydrogen evolution

Nowadays, energy shortage is one of the most challenging issues, particularly in a clean and sustainable way. Hydrogen, as one of the

most promising renewable energy sources, can be generated from water splitting under visible-light irradiation.<sup>201, 202</sup> COFs with diverse structural regularity, crystallinity and porosity are considered as promising photocatalytic hydrogen production platforms.<sup>130, 203-205</sup> Up to now, the highest photocatalytic hydrogen evolution rate of 19120 μmol h<sup>-1</sup> g<sup>-1</sup> was reported by Tan and co-workers based on *ter*-CTF-0.7, which was synthesized from 4,7-bis(4-formylphenyl)-2,1,3-benzothiadiazole (M-BT), 3,6-dicarbaldehyde-N-ethylcarbazole (M-CBZ), and terephthalimidamide dihydrochloride.<sup>206</sup>

The COF first used for photocatalytic hydrogen production was reported in 2014.<sup>35</sup> The triazine-based building block was selected because of its high electron mobility and electron-withdrawing characteristic.<sup>207</sup> Specifically, the crystalline hydrazone-linked COF (TFPT-COF) was prepared by condensation of 2,5-diethoxyterephthalohydrazide with TFPT. Then, Pt as a proton reduction catalyst and TFPT-COF as the photosensitizer were integrated to form TFPT-COF/Pt photocatalyst for visible-light-induced hydrogen evolution with sodium ascorbate or TEOA as an electron donor. A hydrogen evolution rate of 1970 μmol h<sup>-1</sup> g<sup>-1</sup> was achieved with 10 vol% TEOA, which was nearly 3 times higher than other outstanding photocatalytic systems including crystalline poly(triazine imide) and Pt-modified amorphous melon.<sup>36</sup> Moreover, the quantum efficiency was determined to be 2.2 % at 500 nm. Interestingly, on the one hand, TFPT-COF with retained photoactivity lost its crystallinity after 92 h photocatalytic reaction, probably due to its exfoliation in the process; on the other hand, this filtered amorphous product could be easily reconverted to the crystalline TFPT-COF just by putting it under the original experiment conditions without additional new building units,

which suggested that the connectivity and photoactivity of TFPT-COF was retained.

As discussed before, one of the most intriguing characters of COFs is structural tuneability, which allows for structure-to-function design at an atomic level. Indeed, many kinds of researches about COF-based photocatalysts for water splitting have been studies by tailoring the building blocks and linkages. For instance, a series of planar pyrene-based A-TEBPY-COFs was designed and synthesized by extending alkynes with the variation of phripheral heteromatic building units.<sup>181</sup> The visible-light-driven hydrogen production by COF photocatalyst was studied by using Pt as co-catalyst and 10 vol% TEOA as a sacrificial electron donor. A-TEBPY-COF constructed from 1,3,6,8-tetrakis(4-ethynylbenzaldehyde)-pyrene (TEBPY) and hydrazine with the lowest nitrogen content and thereby the most advanced donor features, exhibited the highest hydrogen production rate of  $98 \mu\text{mol h}^{-1} \text{g}^{-1}$  in this system. The results were in accordance with an increasing thermodynamic driving force for hydrogen reduction with decreasing nitrogen content.

Previous studies revealed that rigid, planar dibenzo[b,d]ethiophene sulfone (DBTS) unit was conducive to visible-induced photocatalytic evolution.<sup>208</sup> The DBTS unit was incorporated into ordered COFs to investigate their photocatalytic activity.<sup>124</sup> The as-prepared FS-COF exhibited a high hydrogen generation rate, up to  $16300 \mu\text{mol h}^{-1} \text{g}^{-1}$ , which is almost ten times higher than  $\text{N}_3\text{-COF}$ . Later, three ketoenamine-based COFs were prepared to investigate the effect of different groups on photocatalytic performance.<sup>209</sup> Specifically, TpPa-COF-X (X = -H, -(CH<sub>3</sub>)<sub>2</sub>, and -NO<sub>2</sub>) were constructed from the same host backbone with different functional groups anchored on the framework. In the photocatalytic experiment, H<sub>2</sub> evolution efficiency decreased in the order of TpPa-COF-(CH<sub>3</sub>)<sub>2</sub> > TpPa-COF > TpPa-COF-NO<sub>2</sub>. The order was attributed to the electron-donating ability of three groups, -CH<sub>3</sub> > -H > -NO<sub>2</sub>, which resulted in more efficient charge transferring within the COFs framework. Besides, Benzotriazole as the electron-withdrawing units and thiophene as the electron-donating moieties were selectively introduced into CTFs.<sup>180</sup> The as-prepared CTF-BT/Th was dispersed in water containing 3 wt% Pt as a co-catalyst and 10 vol% TEOA as a sacrificial agent under the visible-light irradiation, exhibiting a maximum hydrogen evolution rate of  $6600 \mu\text{mol h}^{-1} \text{g}^{-1}$  and an AQE of 7.3% at 420 nm. Notably, the AQE was the highest value as compared to the existed triazine-based polymer photocatalysts at that time. To further enhance the activity, attractive COF-based hybrid material was prepared based on benzoic acid-modified CTF-1 (B-CTF-1) and NH<sub>2</sub>-MIL-125(Ti) or NH<sub>2</sub>-UiO-66(Zr).<sup>210</sup> The results showed that the hydrogen evolution rate over 15 wt% NH<sub>2</sub>-MIL-125(Ti)/B-CTF-1 (15TBC) was  $360 \mu\text{mol h}^{-1} \text{g}^{-1}$  under visible light irradiation, which was twice higher than that of the B-CTF-1. This enhanced photocatalytic activity of the 15TBC could be ascribed to the appearance of amide bonds between MOFs and B-CTF-1, which facilitated the charge separation and improved the photocatalyst stability.

Notably, considering the charge recombination and the kinetic overpotential for hydrogen production, there is no evidence for current COFs to produce H<sub>2</sub> without a co-catalyst. Metallic Pt with

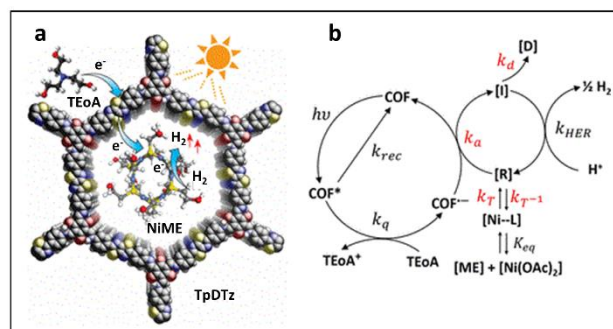


Fig. 12 (a) General schematic of the proposed pathway for H<sub>2</sub> evolution. (b) Proposed key steps of the photocatalytic H<sub>2</sub> evolution reaction with TpDTz COF and NiME cluster cocatalyst. [Ni-L] denotes a ligand-coordinated co-catalyst state which is attained fast compared to the [R] state, [R] denotes the catalyst resting state, which is catalytically active nickel cluster species, [D] denotes the deactivated species, and [I] denotes an intermediate reduced catalyst species able to run the HER step. Reproduced with permission from ref. 123. Copyright 2019, American Chemical Society.

large work function has been widely used for electrons trapping among photocatalysis, which also provides efficient proton reduction sites, making the facile H<sub>2</sub> formation.<sup>211</sup> Thus, the COF backbone with Pt coordination sites enables the specific interaction of COF and Pt, leading to the enhanced charge transfer. However, the stability of Pt in this environment limits its development.<sup>212, 213</sup> Developing earth-abundant, stable, low-cost co-catalysts, which is water-soluble and can also interact with heterogeneous photoabsorber is urgent. Apart from Pt, MoS<sub>2</sub> quantum dots (QDs) with high quantum confinement and small size effect also represent a prominent candidate as the hydrogen generation co-catalyst.<sup>214, 215</sup> MoS<sub>2</sub> QDs modified CTFs (MoS<sub>2</sub>/CTFs) composites was reported to yield higher photocatalytic hydrogen production from water under visible-light illumination. MoS<sub>2</sub> QDs were easily distributed on the surface of CTFs uniformly via an in-situ photo-deposition method.<sup>216</sup> The obtained MoS<sub>2</sub>/CTFs composites showed obviously enhanced photocatalytic hydrogen evolution compared to original CTFs and MoS<sub>2</sub>/g-C<sub>3</sub>N<sub>4</sub> composite. This high activity was ascribed to the interactions between CTFs and MoS<sub>2</sub>, which enabled the efficient electron-hole transfer and separation. Cobaloximes, as the most efficient transition metal-based co-catalyst, features easy synthesis, low overpotentials for hydrogen evolution, and can be easily introduced into the photocatalytic system.<sup>217</sup> Lotsch and co-workers firstly selected noble-metal-free cobaloximes as a co-catalyst in the N<sub>2</sub>-COF-based photocatalytic proton reduction.<sup>218</sup> Several factors influenced the H<sub>2</sub> evolution rate including the solvent, sacrificial donor, reaction pH, and the fundamental properties of COFs such as crystalline and porosity. By selecting azine-linked N<sub>2</sub>-COF as the photosensitizer, chloro(pyridine)cobaloxime as the co-catalyst, and TEOA as a sacrificial donor, H<sub>2</sub> evolution rate of  $782 \mu\text{mol h}^{-1} \text{g}^{-1}$  and TON of 54.4 were obtained in a mixture of water and acetonitrile. Herein electrons were transformed from the LUMO of COF to the co-catalyst, following a monometallic pathway of H<sub>2</sub> evolution from the Co<sup>III</sup>-hydride and/or Co<sup>II</sup>-hydride species. As cobaloxime tends to be inactive within few hours owing to decomposition or hydrogenation, an earth-abundant, noble-metal-free nickelthiolate hexameric cluster was further employed.<sup>123</sup> A visible-light-induced hydrogen

evolution system was constructed with TzDTz COF (TpDTz: Tp and 4,4'-(thiazolo[5,4-d]thiazole-2,5-diyl)dianiline) as a photosensitizer, Ni-thiolate cluster (NiME) as a co-catalyst, and TEOA as a sacrificial agent (Fig. 13). As a result, sustained high  $\text{H}_2$  evolution rate of  $941 \mu\text{mol h}^{-1} \text{g}^{-1}$  and a  $\text{TON}_{\text{Ni}} > 103$  were observed over 70 h visible-light illumination.

## 5.2. Application in photocatalytic oxygen evolution

As mentioned above, great efforts have been made to realize the water photoreduction half-reaction by using COFs as photocatalyst. However, water oxidation for oxygen evolution with a more complicated four-electron redox process is the rate-determining step in overall water splitting, which involves the cleavage of O-H bond, the formation of O-O band, and large overpotential with sluggish O-O formation kinetics.<sup>219, 220</sup> Thus, the researches of photocatalytic water oxidation with COF photocatalysts are far less than that for photocatalytic hydrogen evolution. Emerging examples for photocatalytic oxygen evolution are CTFs reported by Tang et al.,<sup>128, 221</sup>  $\text{sp}^2$  carbon-conjugated COFs developed by Jiang et al. and Zhang et al.,<sup>130, 131, 222</sup> and imine-linked bipyridine COFs prepared by Yang and co-workers.<sup>223</sup> For instance, CTF-1 was synthesized via microwave-assisted condensation at different powers, and then was applied to water splitting.<sup>74</sup> The oxygen evolution from the water was performed by using  $\text{AgNO}_3$  as a sacrificial electron acceptor and  $\text{RuO}_x$  as a co-catalyst. With the visible-light illumination, the highest oxygen evolution rate of  $\text{ca. } 140 \mu\text{mol h}^{-1} \text{g}^{-1}$  was obtained by 3 wt%  $\text{RuO}_x/\text{CTF-1-100W}$ . Notably, the photocatalytic activity of CTF-1-100W without a co-catalyst was even 3 times higher than that of  $\text{g-C}_3\text{N}_4$  with  $\text{RuO}_x$  co-catalyst and 20 times better when CTF-1-100W was decorated a  $\text{RuO}_x$  co-catalyst. The AQE for oxygen production was further determined to be  $\text{ca. } 3.8\%$  at 420 nm. These results suggested the considerable potential of CTFs for photocatalytic oxygen evolution under visible-light irradiation. Meanwhile, 2.01 wt%  $\text{Pt}/\text{CTF-1-100W}$  showed a high hydrogen production of  $5500 \mu\text{mol h}^{-1} \text{g}^{-1}$  with Pt as a co-catalyst and TEOA as a sacrificial electron donor under visible light irradiation ( $\lambda \geq 420 \text{ nm}$ ). CTF-0 based on 1,3,5-tricyanobenzene possessed the highest nitrogen to carbon ratio with alternative benzene and triazine units, which provided more active sites for oxidation reactions. Microwave-assisted synthesis and ionothermal synthesis were also used to produce CTF-0-M and CTF-0-I, respectively.<sup>221</sup> The results suggested that the sample synthesized via ionothermal synthesis (e.g. CTF-0-I) showed a higher oxygen production. Under full arc and visible-light irradiation, CTF-0-I with  $\text{Ag}^+$  as the electron scavenger exhibited the oxygen generation of 226 and  $59 \mu\text{mol g}^{-1}$  in the first hour, respectively. Recently, a bipyridine COF (Bp-COF) has been investigated as the first imine COFs for visible-light-induced water oxidation.<sup>223</sup> The Bp-COF with visible light absorption and appropriate band gap position achieved continuous oxygen generation at a rate of  $152 \mu\text{mol h}^{-1} \text{g}^{-1}$ , corresponding to the AQE of 0.46% at 420 nm, in the presence of  $\text{Co}^{2+}$  as a co-catalyst and  $\text{AgNO}_3$  as an electron acceptor. Although the oxygen production of reported COFs was lower than some inorganic semiconductors and MOF-based catalysts, these results show

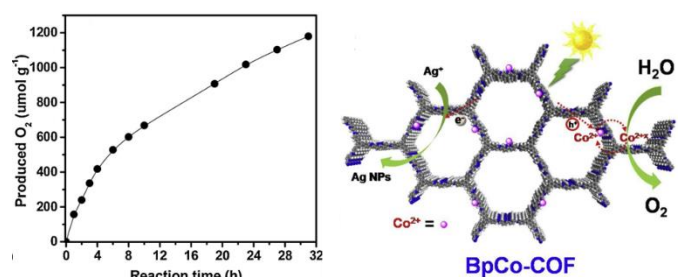


Fig. 13 Photocatalytic  $\text{O}_2$  evolution of BpCo-COF under visible light irradiation ( $\lambda \geq 420 \text{ nm}$ ). Reproduced with permission from ref. 223. Copyright 2020, Elsevier B. V.

the potential of COFs for oxygen evolution, and the photocatalytic activity of COFs for oxygen evolution could be further enhanced by precisely controlling the structural configuration to achieve suitable photoelectric properties.

## 5.3. Application in the reduction of carbon dioxide

With the fast-growing population and global economy, the increasing fossil fuel consumption leads to the excess emission of carbon dioxide ( $\text{CO}_2$ ), which causes serious environmental problems like the greenhouse effect.<sup>224–226</sup> Many solutions such as amines and ionic liquids adsorption, oxy-fuel combustion, and carbonate looping have been put forward pertaining to this dilemma.<sup>227–229</sup> In recent years, photocatalytic reduction of  $\text{CO}_2$  to clean hydrocarbon fuels as an attractive strategy to address the environment and energy issues at the same time has aroused great interest. COFs, the promising photocatalytic candidates, with their high  $\text{CO}_2$  adsorption capacity and selectivity, are recognised as a dramatic platform for photocatalytic reduction of  $\text{CO}_2$ .

Azine-based COFs with the existence of  $\pi$ -stacking aromatic units has been regarded as one of the most attractive candidates for photocatalysis. A large conjugated structure could facilitate the separation and transfer of photo-induced electrons/holes. Recently, two azine-linked crystalline COFs ACOF-1 (hydrazine, TFB) and  $\text{N}_3$ -COF were utilized as photocatalysts for visible-light-induced reduction of  $\text{CO}_2$  with  $\text{H}_2\text{O}$  as a hole scavenger.<sup>126</sup> Understandably, in the reaction of  $\text{CO}_2$  photoreduction, the  $\text{CO}_2$  adsorption capability of the catalyst is the key point. In this study, the high surface area of ACOF-1 ( $1053 \text{ m}^2 \text{g}^{-1}$ ) and  $\text{N}_3$ -COF ( $1412 \text{ m}^2 \text{g}^{-1}$ ) with abundantly accessible nitrogen sites rendered them with high  $\text{CO}_2$  adsorption, leading to the facilitated photocatalytic reduction of  $\text{CO}_2$  to  $\text{CH}_3\text{OH}$ . Upon 24 h visible light irradiation, the total amounts of  $\text{CH}_3\text{OH}$  generated over  $\text{N}_3$ -COF was  $13.7 \mu\text{mol g}^{-1}$ , which was much higher than that of ACOF-1 ( $8.6 \mu\text{mol g}^{-1}$ ). Compared with ACOF-1,  $\text{N}_3$ -COF with electron-poor triazine moieties was able to stabilize the negative charge generated on COF which was important for the enhanced photocatalytic activity. It should be noted that the activity of these COFs outperformed other materials such as  $\text{g-C}_3\text{N}_4$  ( $4.8 \mu\text{mol g}^{-1}$ ) under similar reaction conditions.<sup>230, 231</sup> Furthermore, the electronic properties and configuration of  $\text{N}_3$ -COF and ACOF-1 were



calculated with density functional theory (DFT). The results suggested that the potential of their LUMO was enough to drive CO<sub>2</sub> reduction although the band gap was not suitable for the visible light response. Under visible light irradiation, the excited electrons at the LUMO energy level could reduce the adsorbed CO<sub>2</sub> on the catalyst surface to produce methanol.

Apart from using COF itself as a photocatalyst for the reduction of CO<sub>2</sub>, crystalline COFs have also been considered as a photosensitive supporter to stabilize metallic active moieties for CO<sub>2</sub> conversion.<sup>232</sup> Rhenium(I) bipyridine (bpy) complexes are widely used in constructing photocatalyst to selectively reduce CO<sub>2</sub> into CO under visible light irradiation.<sup>233, 234</sup> A pyridine-based CTF, namely CTF-py, constructed from 2,6-dicyanopyridine (DCP) with abundant N,N-chelating sites allowed for coordination of rhenium complexes targeting for CO<sub>2</sub> photoreduction. A CTF-py was firstly synthesized via traditional trimerization reaction, and then rhenium complex Re(CO)<sub>5</sub>Cl was introduced into the nitrogen sites of CTF-py to obtain Re-CTF-py through the post-synthetic modification.<sup>188</sup> The photocatalytic CO<sub>2</sub> conversion was investigated in a solid-gas system under the irradiation of UV-Vis light, which could avoid dimerization and leaching of reactive species. The production of CO linearly increased with the irradiation time. The highest CO production rate of 353.05  $\mu\text{mol g}^{-1} \text{h}^{-1}$  was observed on Re-CTF-py after 10 h continuous irradiation, while that of pristine CTF-py and the physical mixture were only 13.4  $\mu\text{mol g}^{-1} \text{h}^{-1}$  and 156.2  $\mu\text{mol g}^{-1} \text{h}^{-1}$ , respectively. The photogenerated electrons could easily transfer from CTF-py to Re via the coordination bond, indicating the efficient separation of photo-induced carriers. Using a similar strategy, triazine COF derived from the condensation of 4,4',4''-(1,3,5-triazine-2,4,6-triyl)trianiline (TTA) and 2,2-bipyridyl-5,5-dialdehyde was selected as a photosensitizer to incorporate with Re complex (Re(bpy)(CO)<sub>3</sub>Cl) for photocatalytic conversion of CO<sub>2</sub> to CO.<sup>14</sup> Using Xe lamp as a light source ( $\lambda \geq 420 \text{ nm}$ ) and TEOA as an electron donor, the resulting Re-COF showed a steadily CO generation of 15 mmol/g for more than 20 h after 15 min induction period with a TON of 48, which was 22 times better than its homogeneous Re(bpy)(CO)<sub>3</sub>Cl.

Very recently, COFs were also developed as functional supporters, like TpBpy COF, to anchor active sites for photocatalytic CO<sub>2</sub> conversion.<sup>235-237</sup> Compared with TpBpy, the introduction of Ni resulted in a red-shifted absorption edge and narrower band gap due to the increased delocalization. Moreover, Ni-TpBpy helped to enhance the CO<sub>2</sub> adsorption capacity and isosteric heats, which could be ascribed to the Lewis acid-base interaction between adsorbed CO<sub>2</sub> molecules and loaded Ni ions.<sup>217</sup> In the experiment of Ni-TpBpy photocatalytic CO<sub>2</sub> reduction, [Ru(bpy)<sub>3</sub>]Cl acted as a photosensitizer and TEOA served as an electron donor. Upon illumination, Ru(bpy)<sub>3</sub><sup>2+</sup> was excited and transferred electrons to reduce the coordinated CO<sub>2</sub> molecules on Ni-TpBpy (Fig. 14). The affinity of CO<sub>2</sub> on Ni sites over H<sup>+</sup> was crucial for the inhibition of H<sub>2</sub> formation. As a result, the generated amount of H<sub>2</sub> and CO from Ni-TpBpy catalytic system were 170 and 4057  $\mu\text{mol g}^{-1}$  within 5 hours, respectively, indicating a higher selectivity to CO. This CO production was comparable to other previous reported MOFs and COFs. Control experiments revealed

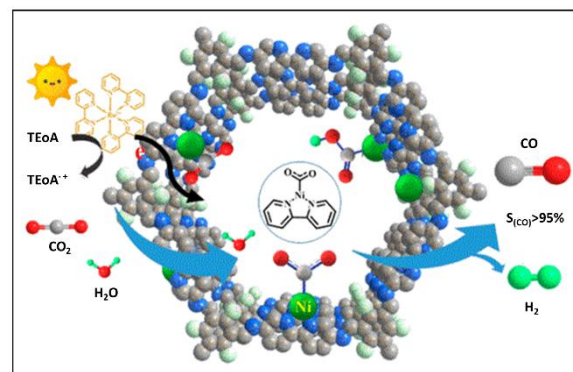


Fig. 14 Schematic diagram photocatalytic selective reduction of CO<sub>2</sub> over Ni-TpBpy. Reproduced with permission from ref. 217. Copyright 2019, American Chemical Society.

that single Ni sites in TpBpy framework acted as catalytic sites while TpBpy facilitated the activity as well as selectivity as a functional support.

#### 5.4. Application in the degradation of pollutants

The unscrupulous discharge of raw sewage into environment has led to a huge threat to ecological systems and human health. Organic pollutant, such as dyes, antibiotics and fertilizers, was one of the most persistent components to be degraded. Among various technologies,<sup>205, 236</sup> photocatalysis utilizing the most abundant solar energy is recognized to be an environmental, sustainable and effective technology for the decomposition of organic contaminants to non-hazardous products.<sup>2, 238, 239</sup> Various kinds of photocatalysts such as TiO<sub>2</sub>,<sup>240, 241</sup> CdS,<sup>9, 242</sup> BiOCl,<sup>243, 244</sup> and g-C<sub>3</sub>N<sub>4</sub><sup>16, 245</sup> have been extensively studied. However, the limited structural and functional tunability hinders their development. For example, g-C<sub>3</sub>N<sub>4</sub> based on triazine or heptazine units offers limited chemical variety and is hard for systematic post-modification. In this regard, COFs with remarkable structural regularity were supposed to be an intriguing platform for photocatalytic degradation of pollutants such as RhB, methyl blue (MB), methyl orange (MO), tetracycline (TC).

Considering the similar features of nitrogen-rich rings and  $\pi$ -conjugated structure to g-C<sub>3</sub>N<sub>4</sub>, COFs with visible-light catalytic active moiety C<sub>3</sub>N<sub>4</sub> exhibited great potential to become a qualified photocatalyst. Over the years, triazine-based COFs have been explored to perform superior photodegradation efficiency, compared with g-C<sub>3</sub>N<sub>4</sub>.<sup>246-248</sup> Likewise, ultrastable TpMA with C<sub>3</sub>N<sub>4</sub> active center was synthesized by the co-condensation of Tp and MA under solvothermal condition, which involved a two-step path of reversible Schiff-base reaction and irreversible enol-keto tautomerization.<sup>248</sup> This subtly designed structure endowed TpMA with the enhanced light-harvesting capability and photooxidation property as a result of the reduced band gap and positive-shifted VB position. MO was selected as a model pollutant to assess the photocatalytic performance of TpMA under visible-light illumination. MO molecules could be degraded with TpMA photocatalyst within 40 min, whereas the bulk g-C<sub>3</sub>N<sub>4</sub> photocatalytic system found almost no degradation under the same conditions. In order to exclude the



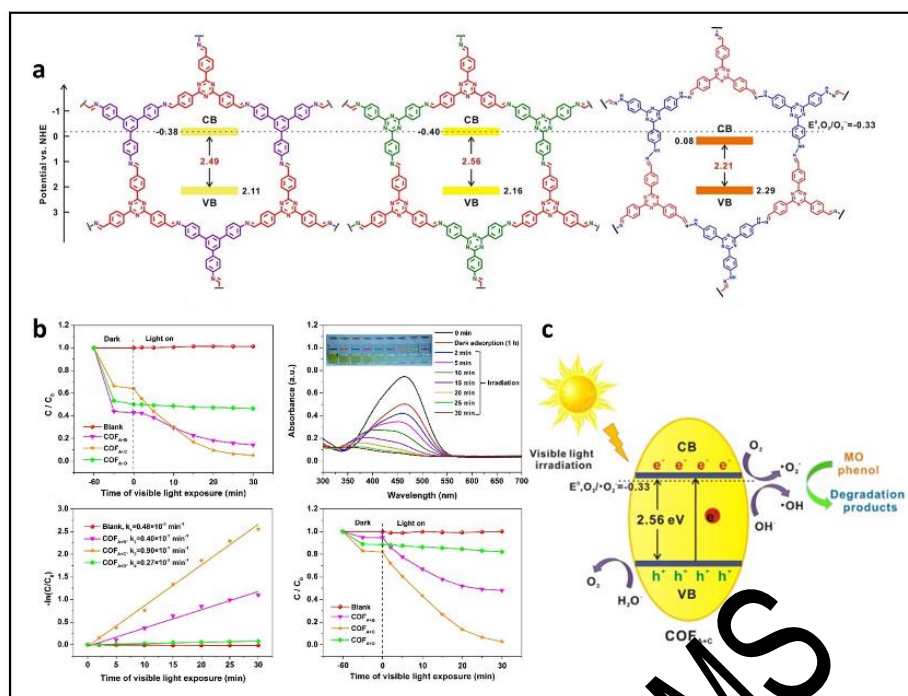


Fig. 15 (a) structure and band alignment of COF<sub>A+B</sub>, COF<sub>A+C</sub> and COF<sub>A+D</sub>. (b) Photocatalytic performance of COF<sub>A+B</sub>, COF<sub>A+C</sub> and COF<sub>A+D</sub> under visible light irradiation (c) schematic illustration of pollutants photodegradation over COF<sub>A+C</sub> under visible light irradiation. Reproduced with permission from ref. 252. Copyright 2017, Elsevier B. V.

photosensitive effect, colorless organic contaminant phenol was also chosen to evaluate the photocatalytic performance of TpMA. Notably, 90 % of phenol was decomposed by TpMA in comparison with 8 % decomposition by g-C<sub>3</sub>N<sub>4</sub> after 40 min irradiation. Upon visible light irradiation, TpMA could be excited when the energy was greater than or equal to its band gap (2.30 eV). Then the dissolved O<sub>2</sub> quickly captured the electrons from CB to obtain O<sub>2</sub><sup>-</sup> (E<sup>0</sup>(O<sub>2</sub>/O<sub>2</sub><sup>-</sup>) = 0.33 eV vs. NHE),<sup>249-251</sup> and the obtained O<sub>2</sub><sup>-</sup> radicals reacted with H<sub>2</sub>O to further produce active OH•. Consequently, MO molecules could be effectively oxidized and mineralized by reactive oxygen species O<sub>2</sub><sup>-</sup> and OH•. According to the total organic carbon (TOC) measurements, TpMA achieved 36.7% of MO mineralization after a 40 min-irradiation.

Recently, three imine-linked COFs with visible-light catalytic active triazine ring were prepared by condensation of three different nitrogen-contained building blocks with the same aldehyde A 4,4',4''-(1,3,5-triazine-2,4,6-triyl)tribenzaldehyde, which yielded COF<sub>A+B</sub>, COF<sub>A+C</sub>, COF<sub>A+D</sub>, separately. Specifically, three different monomers were 1,3,5-tris(4-aminophenyl)benzene (B), 4,4',4''-(1,3,5-triazine-2,4,6-triyl)trianiline (C), and 2,4,6-tris(4-hydrazinylphenyl)-1,3,5-triazine (D) (Fig. 15a).<sup>252</sup> MO dye and colorless phenol as model pollutants were selected to assess the photocatalytic performance of the as-prepared COFs. The BET surface area and the corresponding pore volume followed the similar trend as COF<sub>A+D</sub> (458 m<sup>2</sup> g<sup>-1</sup>, 0.434 cm<sup>3</sup> g<sup>-1</sup>) < COF<sub>A+B</sub> (907 m<sup>2</sup> g<sup>-1</sup>, 0.436 cm<sup>3</sup> g<sup>-1</sup>) < COF<sub>A+C</sub> (1903 m<sup>2</sup> g<sup>-1</sup>, 0.455 cm<sup>3</sup> g<sup>-1</sup>). Although the large surface area and accessible porous nature are beneficial to mass transfer,<sup>112, 253</sup> the interaction between adsorbent-adsorbate should be taken into high priority, especially in the liquid phase. In the case of COF<sub>A+D</sub>, it exhibited higher adsorption

activity than the other two COFs due to the existence of H-bonding between azo groups of MO and hydrazine groups of COF<sub>A+D</sub>. A similar phenomenon was also observed with phenol since the N-containing group could interact with the hydroxyl groups of phenol. Therefore, the adsorption of MO and phenol followed the reverse trend as the BET surface area, as COF<sub>A+B</sub> > COF<sub>A+D</sub> > COF<sub>A+C</sub>. MO molecules could be completely degraded by COF<sub>A+C</sub> under 30 min visible light irradiation, while only 29.6 % MO could be removed by COF<sub>A+B</sub>, and COF<sub>A+D</sub> observed almost no degradation. Similarly, the photocatalytic degradation of phenol followed the order of COF<sub>A+C</sub> > COF<sub>A+B</sub> > COF<sub>A+D</sub> (Fig. 15b). The hydrazine groups on COF<sub>A+D</sub> broke the  $\pi$ -delocalized electron system, leading to the reduction of electron-transfer conductivity and decreasing the interfacial charge transfer; and the CB edge potential of COF<sub>A+D</sub> was too positive to reduce the molecular oxygen to O<sub>2</sub><sup>-</sup> species, resulting in the poor photocatalytic performance. On the other hand, different from COF<sub>A+B</sub>, the interdigitated triazine-benzene heterojunctions in COF<sub>A+C</sub> enabled the decreased electron-hole recombination. As a result, COF<sub>A+C</sub> with a higher density of active centres and conjugation degrees showed the highest photocatalytic performance. COF<sub>A+C</sub> was excited to generate electrons and holes under visible-light illumination. The dissolved O<sub>2</sub> captured the accumulated electrons to yield abundant O<sub>2</sub><sup>-</sup>, and then obtained O<sub>2</sub><sup>-</sup> further reacted with H<sub>2</sub>O to produce OH•. On the other hand, the holes could easily transfer to water or oxidized pollutants, which enabled the effective charge separation. Thus, the final generated reactive radicals including O<sub>2</sub><sup>-</sup> and OH• could degrade pollutants effectively (Fig. 15c). In addition, COF<sub>A+C</sub> did not show any major loss of the activity after four photocatalytic cycles, indicating its high stability and renewability.

Besides, other functional building units have also been utilized to construct COFs with high photocatalytic performance. For example, heptazine unit was embedded into the framework of CTF (forming PCN-1 and PCN-2), which was demonstrated to possess high photocatalytic performance toward degradation of RhB.<sup>254</sup> In detail, PCN-1 was prepared by the polymerization of melem and 2,4,6-Triformylphloroglucinol using a solvent of dimethyl sulfoxide, whereas PCN-2 with crystalline structure was obtained by incorporating melem moieties into CTF. Compared with the traditional polymer semiconductor *g*-C<sub>3</sub>N<sub>4</sub>, the PCN polymers showed broader absorption wavelength, even extended to the entire visible region. Moreover, the enhanced surface area of PCN-2 ensured for more active surface sites, thereby giving more chance for reactants to access for photoredox reactions. As for the photocatalytic performance, PCN-1 and CTF could degrade RhB within 120 min and 60 min, respectively, while PCN-2 could degrade RhB within 25 min under visible light irradiation. Triptycene with 3D spatial orientation containing three benzene rings is another attractive conjugated building unit for microporous materials synthesis. A triptycene-Based imine-linked covalent organic polymer (TP-COP) was prepared for organic dye degradation.<sup>255</sup> Graphene-like layered TP-COP was achieved by manual grinding of terephthaldehyde and triaminotriptycene at room temperature. The DRS analyst indicated that TP-COF responded to visible light, and a narrow band gap of ~2.49 eV was determined by the Tauc's plot. 95% of RhB degradation efficiency could be achieved within 160 min under sunlight irradiation. Meanwhile, TP-COP possessed remarkable reusability in RhB degradation without any visible performance decay.

In addition to the building blocks design, morphology control has also been regarded as an essential method to optimize catalytic efficiency of photocatalysts.<sup>53, 256, 257</sup> Hollow architectures have been investigated to not only promote the interaction between catalysts and substrates by decreasing thickness of structure but also enhance light absorption by multiple light reflections.<sup>54</sup> As for other morphologies, TpMA with thread-like morphology could be synthesized by ball milling varied with the adding amounts of liquid during the process.<sup>134</sup> With the addition of *p*-toluenesulfonic acid and 1 mL solvents, crystalline TpMA<sub>C(1 mL)</sub> was achieved with the well-defined morphology of interwoven thread shape. When the solvent volume was increased to 3 mL, crystalline TpMA<sub>C(3 mL)</sub> with thin ribbon-like morphology was presented. Both TpMA<sub>C(3 mL)</sub> and TpMA<sub>C(1 mL)</sub> were able to respond to visible light and the optical band gap of TpMA<sub>C(3 mL)</sub> and TpMA<sub>C(1 mL)</sub> was 2.29 eV and 2.56 eV, respectively. 10 mg L<sup>-1</sup> phenol as a model environmental contaminant was selected to evaluate the photocatalytic performance of TpMA<sub>C(3 mL)</sub> and TpMA<sub>C(1 mL)</sub>. Consequently, phenol was completely decomposed after 60 min over TpMA<sub>C(3 mL)</sub> under visible light irradiation, while only 83.5 % phenol was degraded by TpMA<sub>C(1 mL)</sub>.<sup>189, 199, 200, 258</sup>

Except for the morphology control, heterojunction construction has also been used to improve the photocatalytic degradation performance of COFs. For example, a Z-scheme MOF/COF heterojunction was firstly reported by the incorporation of NH<sub>2</sub>-MIL-

125(Ti) with TTB-TTA (TTB: 4,4',4''-(1,3,5-triazine-2,4,6-triyl)tribenzaldehyde).<sup>258</sup> The NH<sub>2</sub>-MIL-125(Ti)/TTB-TTA composite exhibited enhanced photocatalytic performance for MO degradation because of efficient charge separation through the covalent heterojunction interface. In addition, BiOBr/CTF-3D composite was designed and prepared, showing enhanced photocatalytic activity toward antibiotic removal.<sup>199</sup>

## 6. Conclusions and outlook

COFs, as a kind of newly developing crystalline porous materials, possess great potential as photocatalysts. Versatile organic building blocks and various covalent bonds for COF synthesis render them with fascinating tailored functionalities. The light-harvesting antennae and photoactive chromophores can be integrated into the COF backbone which provide a platform to tailor the band gap structure for visible-light adsorption and specific photocatalytic reactions. In addition, the extended in-plane conjugation along with the well-defined interlayer  $\pi$ -stacking structures make COFs with enhanced light-absorbing capacity and accelerated charge carrier mobility. In this review, recent progress and advances relating to the COFs design and their photocatalytic application were presented. A growing number of covalent linkages amenable to structure and property design was briefly summarized, and controllable morphologies including 0D structures, 1D structures, 2D structures as well as 3D structures were described. Moreover, strategies for enhancing the photocatalytic activity of COF materials were discussed. In addition, the main applications of COFs as photocatalysts regarding photocatalytic H<sub>2</sub> evolution, CO<sub>2</sub> reduction and photo-degradation of pollutants were presented. While some intriguing progress and achievement have been made, the study of COFs and COF-based photocatalysts is still at its infancy stage and several issues should be solved for future development.

(1). The structures, morphologies and properties of COFs are most likely to be changed with different synthesis methods and reaction conditions, thereby leading to the different photocatalytic performance of COFs. Synthetic strategies such as solvothermal synthesis,<sup>259, 260</sup> ionothermal synthesis,<sup>261, 262</sup> microwave synthesis<sup>74, 221, 263, 264</sup> and room temperature synthesis<sup>265, 266</sup> have been developed for COFs synthesis. While solvothermal synthesis is the most widely used method, the harsh synthesis conditions such as long reaction time, high temperature and pressure, making it difficult for large-scale production. Ionothermal synthesis here is utilized for the synthesis of photoactive triazine core, but the high reaction temperature and low crystalline products hamper the development. The microwave-assisted method and room temperature reaction seem to be better choices. However, only a few examples were reported,<sup>74, 221, 263-265</sup> thus further improvement is needed. Hence, operative, low cost but effective synthetic methods with mild reaction conditions are eager to be introduced for the development of COFs with enhanced photocatalytic activity.

(2). New stable COFs with high efficiency are necessary. How to facile control the band gap structure of COFs should be taken seriously. Efficient utilization of solar spectrum is a significant prerequisite for photocatalysis, and efforts must be made to broaden the light absorption. Besides, the molar absorption coefficient, as a representative factor of the light absorption at a specific wavelength, is highly connected to the photocatalytic activity that photocatalysts with high molar absorption coefficient are able to utilize sunlight more effectively and generate more electron-hole pairs. Thus, constructing COF photocatalysts with enlarged light absorption as well as high molar absorption coefficient is encouraged. For example, as learnt from other traditional photocatalysts, long-wavelength-light-responsive building blocks such as lanthanide-based molecules and phthalocyanine units could be incorporated into COFs to extend the light absorption from visible light to NIR light.<sup>267-269</sup> On the other hand, problem still exists in the high recombination rate of photogenerated charge carriers, which retards the effective transfer of electrons and holes. Two-photocatalyst system was found to replace the single photocatalysts in nature to avoid inevitable back reaction. Similarly, Z-scheme systems are preferred considering that the photogenerated electrons and holes tend to be separated on divided subsystems, which minimizes the possibility of the electron-hole recombination and enables longer-lived charge carriers.

(3). The fundamental mechanism of the COF-based photocatalytic system still remains unclear. Theoretical calculation as a very useful tool is capable of predicting the structures and properties as well as simulating the photocatalytic process. Physicochemical properties of COFs pertaining to the high photocatalytic activity, including surface area, crystallinity, conjugated structure, band gap configuration visible-light absorption, charge separation and transfer should be fully investigated. For example, by the utilization of first-principle calculation, three 2D-CTF models CTF-0,<sup>63</sup> CTF-1,<sup>62</sup> and CTF-2<sup>64</sup> were investigated including electronic band structures, conduction band minimum (CBM)/ valence band maximum (VBM) position, work functions, and optical absorption spectra.<sup>270</sup> As a result, 2D-CTFs with controllable construction are better candidates for visible-light-induced water splitting, which stimulated the experimental research for their photocatalytic properties. Besides, advance characterizations, especially in-situ and even operando technologies should be taken into consideration to reveal the mechanism behind all the photocatalytic processes, which would provide the insight for further development of efficient COFs-based photocatalysts. Technologies such as in-situ FT-IR, in-situ X-ray absorption spectroscopy (XPS) and in-situ extended X-ray absorption fine structure (EXAFS) are highly recommended to monitor the reaction process, distinguishing reactive intermediates and investigating the active sites. More specifically, spectroscopy technologies, such as photoluminescence (PL) spectroscopy, transient absorption (TA) spectroscopy and Kelvin probe force microscopy-based spatially resolved surface photovoltage technique are also needed for the optical and electronic

properties analysis, corresponding to charge carrier transfer and recombination.

(4). Studies of O<sub>2</sub> evolution and CO<sub>2</sub> photoreduction using COF-based photocatalysts should also be strengthened in the near future, they are far less than the researches of H<sub>2</sub> evolution and pollutants degradation. It is a long-term goal to find high performance photocatalysts for visible-light-induced overall water splitting. On the other hand, as for CO<sub>2</sub> photoreduction, increasing the product selectivity demands prompt solutions. Design COFs with highly selective photocatalysis by elaborate selecting functional building blocks and components is highly desired. Additionally, in current photocatalytic systems, uneconomic sacrificial electron donors and cocatalysts, such as TEOA and noble metal Pt, respectively, have often been used. Strategies like reducing the usage or using highly active but economical alternatives are to be achieved for the development of this area. Besides, the photocatalytic activity is known to be affected by varied conditions such as the amount of photocatalyst, the solvent volume, the kind of cocatalysts, the light source and intensity, and the temperature. It is difficult to compare the activity of photocatalysts reported by different groups. The standardization of photocatalytic activity evaluation has become an urgent necessity.

## Conflict of interest

There are no conflicts to declare.

## Acknowledgements

This work was supported by the National Natural Science Foundation of China (No. 51521006, 51709101, 51508177, 51579098, 51579096, 51779090), the National Program for Support of Top-Notch Young Professionals of China (2012, 2014), Hunan Provincial Science and Technology Plan Project (No.2016RS3026, 2017SK2243, 2017SK2241), the Program for Changjiang Scholars and Innovative Research Team in University (IRT-13R17) and the Three Gorges Follow-up Research Project (2017HXXY-05). W. H, L. X. Y and T. J. W are thankful for the financial support from UK EPSRC (EP/N009533/1), Royal Society-Newton Advanced Fellowship grant (NA170422) and the Leverhulme Trust (RPG-2017-122).

## Notes and references

1. R. Fouquet, *Nat Energy*, 2016, **1**, 16098.
2. C. Y. Zhou, C. Lai, C. Zhang, G. M. Zeng, D. L. Huang, M. Cheng, L. Hu, W. P. Xiong, M. Chen, J. J. Wang, Y. Yang and L. B. Jiang, *Appl Catal B-Environ*, 2018, **238**, 6-18.
3. K. He, G. Q. Chen, G. M. Zeng, A. W. Chen, Z. Z. Huang, J. B. Shi, T. T. Huang, M. Peng and L. Hu, *Appl Catal B-Environ*, 2018, **228**, 19-28.
4. F. A., K. Honda, *Nature*, 1972, **238**, 37-38.
5. J. H. Carey, J. Lawrence and H. M. Tosine, *Bull. Environ. Contam. Toxicol.*, 1976, **16**, 697-701.
6. W. Li, A. Elzatahry, D. Aldhayan and D. Y. Zhao, *Chemical Society reviews*, 2018, **47**, 8203-8237.

7. J. Schneider, M. Matsuoka, M. Takeuchi, J. L. Zhang, Y. Horiuchi, M. Anpo and D. W. Bahnemann, *Chemical reviews*, 2014, **114**, 9919-9986.
8. O. Ola and M. M. Maroto-Valer, *J Photoch Photobio C*, 2015, **24**, 16-42.
9. Q. Li, X. Li, S. Wageh, A. A. Al-Ghamdi and J. G. Yu, *Adv Energy Mater*, 2015, **5**, 1500010.
10. J. X. Low, B. Z. Dai, T. Tong, C. J. Jiang and J. G. Yu, *Advanced materials*, 2019, **31**, 1802981.
11. L. Cheng, Q. J. Xiang, Y. L. Liao and H. W. Zhang, *Energy & Environmental Science*, 2018, **11**, 1362-1391.
12. C. B. Ong, L. Y. Ng and A. W. Mohammad, *Renew Sust Energy Rev*, 2018, **81**, 536-551.
13. K. M. Lee, C. W. Lai, K. S. Ngai and J. C. Juan, *Water Res*, 2016, **88**, 428-448.
14. D. J. Martin, G. Liu, S. J. A. Moniz, Y. Bi, A. M. Beale, J. Ye and J. Tang, *Chemical Society Reviews*, 2015, **44**, 7808-7828.
15. M. D. Hernandez-Alonso, F. Fresno, S. Suarez and J. M. Coronado, *Energy & Environmental Science*, 2009, **2**, 1231-1257.
16. J. W. Fu, J. G. Yu, C. J. Jiang and B. Cheng, *Adv Energy Mater*, 2018, **8**, 1701503.
17. S. W. Cao and J. G. Yu, *Journal of Physical Chemistry Letters*, 2014, **5**, 2101-2107.
18. D. N. Jiang, P. Xu, H. Wang, G. M. Zeng, D. L. Huang, M. Chen, C. Lai, C. Zhang, J. Wan and W. J. Xue, *Coordination Chemistry Reviews*, 2018, **376**, 449-466.
19. A. Dhakshinamoorthy, A. M. Asiri and H. Garcia, *Angew Chem Int Edit*, 2016, **55**, 5414-5445.
20. Y. O. Wang, A. Vogel, M. Sachs, R. S. Sprick, L. Wilbraham, S. J. A. Moniz, R. Godin, M. A. Zwiijnenburg, J. R. Durrant, A. I. Cooper and J. W. Tang, *Nat Energy*, 2019, **4**, 746-760.
21. T. Banerjee, K. Gottschling, G. Savasci, C. Ochsenfeld and B. V. Lotsch, *Acs Energy Lett*, 2018, **3**, 400-409.
22. X. Chen, M. Addicoat, E. Q. Jin, L. P. Zhai, H. Xu, N. Huang, Z. Q. Guo, L. L. Liu, S. Irle and D. L. Jiang, *J Am Chem Soc*, 2015, **137**, 3241-3247.
23. G. Q. Lin, H. M. Ding, R. F. Chen, Z. K. Peng, B. C. Wan and C. Wang, *J Am Chem Soc*, 2017, **139**, 8715-8709.
24. X. S. Ding, J. Guo, X. A. Feng, Y. Honsho, D. Guo, S. Seki, P. Maitarad, A. Saeki, S. Nagase and D. L. Jiang, *Angew Chem Int Edit*, 2011, **50**, 1229-129.
25. G. P. Dong, Y. H. Zhang, Q. W. Fan and J. R. Qiu, *J Photoch Photobio C*, 2014, **20**, 33-50.
26. H. Lyu, C. S. Diercks, C. H. Zhu and O. M. Yaghi, *J Am Chem Soc*, 2019, **141**, 6848-6852.
27. S. C. Yan, X. Y. Guan, H. Li, D. H. Li, M. Xue, Y. S. Yan, V. Valtchev, S. L. Qiu and Q. R. Fang, *J Am Chem Soc*, 2019, **141**, 2920-2924.
28. R. F. Chen, J. L. Shi, Y. Ma, G. Q. Lin, X. J. Lang and C. Wang, *Angew Chem Int Edit*, 2019, **58**, 6430-6434.
29. S. Lin, C. S. Diercks, Y. B. Zhang, N. Kornienko, E. M. Nichols, Y. B. Zhao, A. R. Paris, D. Kim, P. Yang, O. M. Yaghi and C. J. Chang, *Science*, 2015, **349**, 1208-1213.
30. P. Das and S. K. Mandal, *Chemistry of Materials*, 2019, **31**, 1584-1596.
31. S. S. Han, H. Furukawa, O. M. Yaghi and W. A. Goddard, *J Am Chem Soc*, 2008, **130**, 11580-+.
32. L. L. Wang, C. Zeng, H. Xu, P. C. Yin, D. C. Chen, J. Deng, M. Li, N. Zheng, C. Gu and Y. G. Ma, *Chemical science*, 2019, **10**, 1023-1028.
33. Z. Meng, R. M. Stolz and K. A. Mirica, *J Am Chem Soc*, 2019, **141**, 11929-11937.
34. S. Wan, J. Guo, J. Kim, H. Ihee and D. L. Jiang, *Angew Chem Int Edit*, 2008, **47**, 8826-8830.
35. L. Stegbauer, K. Schwinghammer and B. V. Lotsch, *Chemical science*, 2014, **5**, 2789-2793.
36. K. Schwinghammer, B. Tuffy, M. B. Mesch, E. Wirnhier, C. Martineau, F. Taulelle, W. Schnick, J. Senker and B. V. Lotsch, *Angew Chem Int Edit*, 2013, **52**, 2435-2439.
37. J. S. Zhang, X. F. Chen, K. Takanabe, K. Maeda, K. Domen, J. D. Epping, X. Z. Fu, M. Antonietti and X. C. Wang, *Angew Chem Int Edit*, 2010, **49**, 441-444.
38. R. P. Bisbey and W. R. Dichtel, *ACS central science*, 2017, **3**, 533-543.
39. P. J. Waller, F. Gandara and O. M. Yaghi, *Accounts Chem Res*, 2015, **48**, 3053-3063.
40. S. Y. Ding and W. Wang, *Chemical Society reviews*, 2013, **42**, 548-568.
41. Y. F. Zeng, R. Q. Zou and Y. L. Zhao, *Advanced materials*, 2016, **28**, 2855-2873.
42. S. S. Yuan, X. Li, Y. Zhu, G. Zhang, P. Van Puyvelde and B. Van der Bruggen, *Chemical Society reviews*, 2019, **48**, 2665-2681.
43. H. Wang, Z. T. Zeng, P. Xu, L. S. Li, G. M. Zeng, R. Xiao, Z. Y. Tang, D. L. Huang, J. Tang, C. Lai, D. N. Jiang, Y. Liu, H. Yi, L. Qin, S. J. Ye, Y. F. Ren and W. W. Tang, *Chemical Society reviews*, 2019, **48**, 488-516.
44. H. Wang, D. Jiang, D. Huang, G. Zeng, P. Xu, C. Lai, M. Chen, M. Cheng, C. Zhang and Z. Wang, *Journal of Materials Chemistry A*, 2019, **7**, 22848-22870.
45. A. P. Cote, A. I. Benin, N. W. Ockwig, M. O'Keeffe, A. J. Matzger and O. M. Yaghi, *Science*, 2005, **310**, 1166-1170.
46. H. M. El-Kaderi, J. R. Hunt, J. L. Mendoza-Cortes, A. P. Cote, R. E. Taylor, M. O'Keeffe and O. M. Yaghi, *Science*, 2007, **316**, 268-272.
47. J. F. Dienstmaier, D. D. Medina, M. Dogru, P. Knochel, T. Bein, W. M. Heckl and M. Lackinger, *ACS nano*, 2012, **6**, 7234-7242.
48. S. Wan, J. Guo, J. Kim, H. Ihee and D. L. Jiang, *Angew Chem Int Edit*, 2009, **48**, 5439-5442.
49. C. H. Liu, W. Zhang, Q. D. Zeng and S. B. Lei, *Chem-Eur J*, 2016, **22**, 6768-6773.
50. B. J. Smith and W. R. Dichtel, *J Am Chem Soc*, 2014, **136**, 8783-8789.
51. B. T. Koo, R. F. Heden and P. Clancy, *Phys Chem Chem Phys*, 2017, **19**, 9745-9754.
52. N. L. Campbell, R. Clowes, L. K. Ritchie and A. I. Cooper, *Chemistry of Materials*, 2009, **21**, 204-206.
53. M. Calik, F. Auras, L. M. Salonen, K. Bader, I. Grill, M. Handloser, D. D. Medina, M. Dogru, F. Lobermann, D. Trauner, A. Hartschuh and T. Bein, *J Am Chem Soc*, 2014, **136**, 17802-17807.
54. S. B. Jin, K. Furukawa, M. Addicoat, L. Chen, S. Takahashi, S. Irle, T. Nakamura and D. L. Jiang, *Chemical science*, 2013, **4**, 4505-4511.
55. E. L. Spitler and W. R. Dichtel, *Nature chemistry*, 2010, **2**, 672-677.
56. N. Huang, L. P. Zhai, D. E. Coupry, M. A. Addicoat, K. Okushita, K. Nishimura, T. Heine and D. L. Jiang, *Nature communications*, 2016, **7**, 12325.
57. S. Dalapati, E. Q. Jin, M. Addicoat, T. Heine and D. L. Jiang, *J Am Chem Soc*, 2016, **138**, 5797-5800.



58. C. Jiang, M. Tang, S. L. Zhu, J. D. Zhang, Y. C. Wu, Y. Chen, C. Xia, C. L. Wang and W. P. Hu, *Angew Chem Int Edit*, 2018, **57**, 16072-16076.
59. S. Wang, L. Ma, Q. Y. Wang, P. P. Shao, D. Ma, S. Yuan, P. Lei, P. F. Li, X. Feng and B. Wang, *J Mater Chem C*, 2018, **6**, 5369-5374.
60. V. Nguyen and M. Grunwald, *J Am Chem Soc*, 2018, **140**, 3306-3311.
61. H. Y. Li, A. D. Chavez, H. F. Li, H. Li, W. R. Dichtel and J. L. Bredas, *J Am Chem Soc*, 2017, **139**, 16310-16318.
62. P. Kuhn, M. Antonietti and A. Thomas, *Angew Chem Int Edit*, 2008, **47**, 3450-3453.
63. P. Katekomol, J. Roeser, M. Bojdys, J. Weber and A. Thomas, *Chemistry of Materials*, 2013, **25**, 1542-1548.
64. M. J. Bojdys, J. Jeromenok, A. Thomas and M. Antonietti, *Advanced materials*, 2010, **22**, 2202-2205.
65. S. Dey, A. Bhunia, D. Esquivel and C. Janiak, *Journal of Materials Chemistry A*, 2016, **4**, 6259-6263.
66. P. Puthiaraj, S. M. Cho, Y. R. Lee and W. S. Ahn, *Journal of Materials Chemistry A*, 2015, **3**, 6792-6797.
67. S. Y. Yu, J. Mahmood, H. J. Noh, J. M. Seo, S. M. Jung, S. H. Shin, Y. K. Im, I. Y. Jeon and J. B. Baek, *Angew Chem Int Edit*, 2018, **57**, 8438-8442.
68. K. W. Wang, L. M. Yang, X. Wang, L. P. Guo, G. Cheng, C. Zhang, S. B. Jin, B. Tan and A. Cooper, *Angew Chem Int Edit*, 2017, **56**, 14149-14153.
69. M. Liu, Q. Huang, S. Wang, Z. Li, B. Li, S. Jin and B. Tan, *Angewandte Chemie*, 2018, **57**, 11968-11972.
70. M. Y. Liu, L. P. Guo, S. B. Jin and B. E. Tan, *Journal of Materials Chemistry A*, 2019, **7**, 5153-5172.
71. X. C. Wang, K. Maeda, A. Thomas, K. Takanabe, G. Xin, J. M. Carlsson, K. Domen and M. Antonietti, *Nature materials*, 2009, **8**, 76-80.
72. A. Mishra, A. Mehta, S. Basu, N. P. Shetti, K. R. Reddy and T. M. Aminabhavi, *Carbon*, 2019, **149**, 693-721.
73. X. Jiang, P. Wang and J. J. Zhao, *Journal of Materials Chemistry A*, 2015, **3**, 7750-7758.
74. J. J. Xie, S. A. Shevlin, Q. S. Ruan, S. J. A. Morris, J. R. Liu, X. Liu, Y. M. Li, C. C. Lau, Z. X. Guo and J. W. Tang, *Energy & Environmental Science*, 2018, **11**, 1617-1624.
75. D. J. Martin, K. P. Qiu, S. A. Shevlin, A. D. Handoko, X. W. Chen, Z. X. Guo and J. W. Tang, *Angew Chem Int Edit*, 2014, **53**, 9240-9245.
76. F. J. Uribe-Romo, J. R. Hunt, H. Furukawa, C. Klock, M. O'Keeffe and O. M. Yaghi, *J Am Chem Soc*, 2009, **131**, 4570-4571.
77. Y. X. Ma, Z. J. Li, L. Wei, S. Y. Ding, Y. B. Zhang and W. Wang, *J Am Chem Soc*, 2017, **139**, 4995-4998.
78. G. Q. Lin, H. M. Ding, D. Q. Yuan, B. S. Wang and C. Wang, *J Am Chem Soc*, 2016, **138**, 3302-3305.
79. S. Y. Ding, J. Gao, Q. Wang, Y. Zhang, W. G. Song, C. Y. Su and W. Wang, *J Am Chem Soc*, 2011, **133**, 19816-19822.
80. S. B. Jin, T. Sakurai, T. Kowalczyk, S. Dalapati, F. Xu, H. Wei, X. Chen, J. Gao, S. Seki, S. Irle and D. L. Jiang, *Chem-Eur J*, 2014, **20**, 14608-14613.
81. T. Y. Zhou, S. Q. Xu, Q. Wen, Z. F. Pang and X. Zhao, *J Am Chem Soc*, 2014, **136**, 15885-15888.
82. Z. F. Pang, S. Q. Xu, T. Y. Zhou, R. R. Liang, T. G. Zhan and X. Zhao, *J Am Chem Soc*, 2016, **138**, 4710-4713.
83. X. Chen, M. Addicoat, E. Q. Jin, H. Xu, T. Hayashi, F. Xu, N. Huang, S. Irle and D. L. Jiang, *Scientific reports*, 2015, **5**, 14650.
84. J. Y. Yue, Y. P. Mo, S. Y. Li, W. L. Dong, T. Chen and D. Wang, *Chemical science*, 2017, **8**, 2169-2174.
85. Y. Z. Liu, Y. H. Ma, Y. B. Zhao, X. X. Sun, F. Gandara, H. Furukawa, Z. Liu, H. Y. Zhu, C. H. Zhu, K. Suenaga, P. Oleynikov, A. S. Alshammari, X. Zhang, O. Terasaki and O. M. Yaghi, *Science*, 2016, **351**, 365-369.
86. S. Wan, F. Gandara, A. Asano, H. Furukawa, A. Saeki, S. K. Dey, L. Liao, M. W. Ambrogio, Y. Y. Botros, X. F. Duan, S. Seki, J. F. Stoddart and O. M. Yaghi, *Chemistry of Materials*, 2011, **23**, 4094-4097.
87. S. Kandambeth, A. Mallick, B. Lukose, M. V. Mane, T. Heine and R. Banerjee, *J Am Chem Soc*, 2012, **134**, 19524-19527.
88. S. Chandra, S. Kandambeth, B. P. Biswal, B. Lukose, S. M. Kunjir, M. Chaudhary, R. Babarao, T. Heine and R. Banerjee, *J Am Chem Soc*, 2013, **135**, 17853-17861.
89. B. P. Biswal, S. Chandra, S. Kandambeth, B. Lukose, T. Heine and R. Banerjee, *J Am Chem Soc*, 2013, **135**, 5328-5331.
90. M. Bhadra, S. Kandambeth, M. K. Sahoo, M. Addicoat, E. Balaraman and R. Banerjee, *J Am Chem Soc*, 2019, **141**, 6152-6156.
91. P. Pachfule, A. Chharjya, J. Roeser, T. Langenhahn, M. Schwarze, R. Schomacker, A. Thomas and J. Schmidt, *J Am Chem Soc*, 2018, **140**, 1413-1427.
92. S. L. Lu, Y. M. Gu, S. Wang, R. McCaffrey, Y. H. Jin, H. W. Gu and W. Zhang, *J Am Chem Soc*, 2017, **139**, 17082-17088.
93. M. R. Rao, Y. Fang, S. De Feyter and D. F. Perepichka, *J Am Chem Soc*, 2017, **139**, 2421-2427.
94. F. Uribe-Romo, C. J. Doonan, H. Furukawa, K. Oisaki and O. M. Yaghi, *J Am Chem Soc*, 2011, **133**, 11478-11481.
95. N. Junck and W. R. Dichtel, *J Am Chem Soc*, 2013, **135**, 14952-14955.
96. L. Gottschling, L. Stegbauer, G. Savasci, N. A. Prisco, Z. J. Berkson, C. Ochsenfeld, B. F. Chmelka and B. V. Lotsch, *Chemistry of Materials*, 2019, **31**, 1946-1955.
97. X. J. Zhao, P. Pachfule, S. Li, T. Langenhahn, M. Y. Ye, C. Schlesiger, S. Praetz, J. Schmidt and A. Thomas, *J Am Chem Soc*, 2019, **141**, 6623-6630.
98. W. T. Liu, Q. Su, P. Y. Ju, B. X. Guo, H. Zhou, G. H. Li and Q. L. Wu, *ChemSusChem*, 2017, **10**, 664-669.
99. S. Dalapati, S. B. Jin, J. Gao, Y. H. Xu, A. Nagai and D. L. Jiang, *J Am Chem Soc*, 2013, **135**, 17310-17313.
100. Y. L. Zhu, S. Wan, Y. H. Jin and W. Zhang, *J Am Chem Soc*, 2015, **137**, 13772-13775.
101. S. B. Alahakoon, C. M. Thompson, A. X. Nguyen, G. Occhialini, G. T. McCandless and R. A. Smaldone, *Chem Commun*, 2016, **52**, 2843-2845.
102. V. S. Vyas, F. Haase, L. Stegbauer, G. Savasci, F. Podjaski, C. Ochsenfeld and B. V. Lotsch, *Nature communications*, 2015, **6**, 8508.
103. F. Haase, T. Banerjee, G. Savasci, C. Ochsenfeld and B. V. Lotsch, *Faraday Discuss*, 2017, **201**, 247-264.
104. Q. R. Fang, Z. B. Zhuang, S. Gu, R. B. Kaspar, J. Zheng, J. H. Wang, S. L. Qiu and Y. S. Yan, *Nature communications*, 2014, **5**, 4503.
105. A. P. Cote, H. M. El-Kaderi, H. Furukawa, J. R. Hunt and O. M. Yaghi, *J Am Chem Soc*, 2007, **129**, 12914-12915.
106. Q. R. Fang, J. H. Wang, S. Gu, R. B. Kaspar, Z. B. Zhuang, J. Zheng, H. X. Guo, S. L. Qiu and Y. S. Yan, *J Am Chem Soc*, 2015, **137**, 8352-8355.
107. Z. Luo, L. Liu, J. Ning, K. Lei, Y. Lu, F. Li and J. Chen, *Angewandte Chemie*, 2018, **57**, 9443-9446.

108. C. L. Zhang, S. M. Zhang, Y. H. Yan, F. Xia, A. N. Huang and Y. Z. Xian, *ACS applied materials & interfaces*, 2017, **9**, 13415-13421.
109. S. J. Lyle, T. M. O. Popp, P. J. Waller, X. K. Pei, J. A. Reimer and O. M. Yaghi, *J Am Chem Soc*, 2019, **141**, 11253-11258.
110. J. R. Hunt, C. J. Doonan, J. D. LeVangie, A. P. Cote and O. M. Yaghi, *J Am Chem Soc*, 2008, **130**, 11872-11873.
111. J. Guo, Y. H. Xu, S. B. Jin, L. Chen, T. Kaji, Y. Honsho, M. A. Addicoat, J. Kim, A. Saeki, H. Ihee, S. Seki, S. Irle, M. Hiramoto, J. Gao and D. L. Jiang, *Nature communications*, 2013, **4**, 2736.
112. A. Nagai, X. Chen, X. Feng, X. S. Ding, Z. Q. Guo and D. L. Jiang, *Angew Chem Int Edit*, 2013, **52**, 3770-3774.
113. K. T. Jackson, T. E. Reich and H. M. El-Kaderi, *Chem Commun*, 2012, **48**, 8823-8825.
114. D. A. Pyles, J. W. Crowe, L. A. Baldwin and P. L. McGrier, *ACS Macro Lett*, 2016, **5**, 1055-1058.
115. Y. H. Cho, C. Y. Lee, D. C. Ha and C. H. Cheon, *Adv Synth Catal*, 2012, **354**, 2992-2996.
116. B. Nath, W. H. Li, J. H. Huang, G. E. Wang, Z. H. Fu, M. S. Yao and G. Xu, *Crystengcomm*, 2016, **18**, 4259-4263.
117. Y. Du, H. S. Yang, J. M. Whiteley, S. Wan, Y. H. Jin, S. H. Lee and W. Zhang, *Angew Chem Int Edit*, 2016, **55**, 1737-1741.
118. H. F. Li, H. Y. Li, Q. Q. Dai, H. Li and J. L. Bredas, *Adv Theor Simul*, 2018, **1**, 1700015.
119. L. M. Lanni, R. W. Tilford, M. Bharathy and J. J. Lavigne, *J Am Chem Soc*, 2011, **133**, 13975-13983.
120. S. Kandambeth, D. B. Shinde, M. K. Panda, B. Lukose, T. Heine and R. Banerjee, *Angew Chem Int Edit*, 2013, **52**, 13052-13056.
121. H. Xu, J. Gao and D. L. Jiang, *Nat Chem*, 2015, **7**, 905-912.
122. Y.-P. Zhang, H.-L. Tang, H. Dong, M.-Y. Gao, C.-C. Li, X.-J. Sun, J.-Z. Wei, Y. Qu, Z.-J. Li and F.-M. Zhang, *Journal of Materials Chemistry A*, 2020, **8**, 4334-4340.
123. B. P. Biswal, H. A. Vignolo-Gonzalez, T. Banerjee, L. Grunenberg, G. Savasci, K. Gottschling, J. Nuss, C. Ochsenfeld and B. V. Lotsch, *J Am Chem Soc*, 2019, **141**, 11082-11092.
124. X. Y. Wang, L. J. Chen, S. Y. Chong, M. A. Little, Y. Z. Wu, W. H. Zhu, R. Clowes, Y. Yan, M. A. Zwirnerburg, J. S. Sprick and A. I. Cooper, *Nat Chem*, 2018, **10**, 1180-1189.
125. L. Stegbauer, S. Zech, G. Savasci, T. Banerjee, F. Podjaski, K. Schwinghammer, C. Ochsenfeld and B. V. Lotsch, *Adv Energy Mater*, 2018, **8**, 1180-1189.
126. Y. H. Fu, X. L. Zhu, L. Huang, X. C. Zhang, F. M. Zhang and W. D. Zhu, *Appl Catal B-Environ*, 2018, **239**, 46-51.
127. S. Z. Yang, W. H. Hu, X. Zhang, P. L. He, B. Pattengale, C. M. Liu, M. Cendejas, I. Hermans, X. Y. Zhang, J. Zhang and J. E. Huang, *J Am Chem Soc*, 2018, **140**, 14614-14618.
128. J. Xie, S. A. Shevlin, Q. Ruan, S. J. A. Moniz, Y. Liu, X. Liu, Y. Li, C. C. Lau, Z. X. Guo and J. Tang, *Energy & Environmental Science*, 2018, **11**, 1617-1624.
129. L. Y. Li, W. Fang, P. Zhang, J. H. Bi, Y. H. He, J. Y. Wang and W. Y. Su, *Journal of Materials Chemistry A*, 2016, **4**, 12402-12406.
130. S. C. Wei, F. Zhang, W. B. Zhang, P. R. Qiang, K. J. Yu, X. B. Fu, D. Q. Wu, S. Bi and F. Zhang, *J Am Chem Soc*, 2019, **141**, 14272-14279.
131. S. Bi, C. Yang, W. B. Zhang, J. S. Xu, L. M. Liu, D. Q. Wu, X. C. Wang, Y. Han, Q. F. Liang and F. Zhang, *Nat Commun*, 2019, **10**, 2467.
132. X. D. Zhuang, W. X. Zhao, F. Zhang, Y. Cao, F. Liu, S. Bia and X. L. Feng, *Polymer Chemistry*, 2016, **7**, 4176-4181.
133. X. L. Li, C. L. Zhang, S. L. Cai, X. H. Lei, V. Altoe, F. Hong, J. J. Urban, J. Ciston, E. M. Chan and Y. Liu, *Nature communications*, 2018, **9**, 2998.
134. H. Z. Lv, X. L. Zhao, H. Y. Niu, S. J. He, Z. Tang, F. C. Wu and J. P. Giesy, *J Hazard Mater*, 2019, **369**, 494-502.
135. H. Y. Liu, J. Chu, Z. L. Yin, X. Cai, L. Zhuang and H. X. Deng, *Chem-Us*, 2018, **4**, 1696-1709.
136. G. Das, B. P. Biswal, S. Kandambeth, V. Venkatesh, G. Kaur, M. Addicoat, T. Heine, S. Verma and R. Banerjee, *Chemical science*, 2015, **6**, 3931-3939.
137. P. Pachfule, S. Kandambeth, A. Mallick and R. Banerjee, *Chem Commun*, 2015, **51**, 11717-11720.
138. S. J. He, T. Zeng, S. H. Wang, H. Y. Niu and Y. Q. Cai, *ACS applied materials & interfaces*, 2017, **9**, 2959-2965.
139. B. J. Smith, L. R. Parent, A. C. Overholts, P. A. Beaucage, R. P. Bisbey, A. D. Chavez, N. Hwang, C. Park, A. M. Evans, N. C. Gianneschi and W. R. Dichtel, *ACS central science*, 2017, **3**, 58-65.
140. A. M. Evans, L. R. Parent, N. C. Flanders, R. P. Bisbey, E. Vitaku, M. S. Firschnner, R. D. Schaller, L. X. Chen, N. C. Gianneschi and W. R. Dichtel, *Science*, 2018, **361**, 53-57.
141. R. L. Li, L. C. Flanders, A. M. Evans, W. Ji, I. Castano, L. X. Chen, N. C. Gianneschi and W. R. Dichtel, *Chemical science*, 2019, **10**, 3756-3761.
142. D. Beydoun, R. Amal, G. Low and S. McEvoy, *Journal of Nanoparticle Research*, 1999, **1**, 439-458.
143. X. F. Fan and C. M. Lieber, *Advanced materials*, 2000, **12**, 298-302.
144. W. Huang, Y. Jiang, X. Li, X. J. Li, J. Y. Wang, Q. Wu and X. K. Liu, *ACS applied materials & interfaces*, 2013, **5**, 8845-8849.
145. Y. Jiang, W. Huang, J. Y. Wang, Q. Wu, H. J. Wang, L. L. Pan and X. K. Liu, *Journal of Materials Chemistry A*, 2014, **2**, 8201-8204.
146. D. Rodriguez-San-Miguel, A. Abrishamkar, J. A. R. Navarro, R. Rodriguez-Trujillo, D. B. Amabilino, R. Mas-Balleste, F. Zamora and J. Puigmarti-Luis, *Chem Commun*, 2016, **52**, 9212-9215.
147. B. Luo, G. Liu and L. Z. Wang, *Nanoscale*, 2016, **8**, 6904-6920.
148. J. Di, J. Xiong, H. M. Li and Z. Liu, *Advanced materials*, 2018, **30**, 1704548.
149. K. Nakata and A. Fujishima, *J Photoch Photobio C*, 2012, **13**, 169-189.
150. S. Ida and T. Ishihara, *Journal of Physical Chemistry Letters*, 2014, **5**, 2533-2542.
151. K. X. Yao, Y. L. Chen, Y. Lu, Y. F. Zhao and Y. Ding, *Carbon*, 2017, **122**, 258-265.
152. I. Berlanga, M. L. Ruiz-Gonzalez, J. M. Gonzalez-Calbet, J. L. G. Fierro, R. Mas-Balleste and F. Zamora, *Small*, 2011, **7**, 1207-1211.
153. I. Berlanga, R. Mas-Balleste and F. Zamora, *Chem Commun*, 2012, **48**, 7976-7978.
154. J. W. Colson, A. R. Woll, A. Mukherjee, M. P. Levendorf, E. L. Spitler, V. B. Shields, M. G. Spencer, J. Park and W. R. Dichtel, *Science*, 2011, **332**, 228-231.
155. Z. Zha, L. Xu, Z. Wang, X. Li, Q. Pan, P. Hu and S. Lei, *ACS applied materials & interfaces*, 2015, **7**, 17837-17843.
156. J. I. Feldblyum, C. H. McCreery, S. C. Andrews, T. Kurosawa, E. J. G. Santos, V. Duong, L. Fang, A. L. Ayzner and Z. N. Bao, *Chem Commun*, 2015, **51**, 13894-13897.

157. K. Dey, M. Pal, K. C. Rout, H. S. Kunjattu, A. Das, R. Mukherjee, U. K. Kharul and R. Banerjee, *J Am Chem Soc*, 2017, **139**, 13083-13091.
158. Y. Chen, H. J. Cui, J. Q. Zhang, K. Zhao, D. F. Ding, J. Guo, L. S. Li, Z. Y. Tian and Z. Y. Tang, *Rsc Adv*, 2015, **5**, 92573-92576.
159. T. Sick, A. G. Hufnagel, J. Kampmann, I. Kondofersky, M. Calik, J. M. Rotter, A. Evans, M. Doblinger, S. Herbert, K. Peters, D. Bohm, P. Knochel, D. D. Medina, D. Fattakhova-Rohlfing and T. Bein, *J Am Chem Soc*, 2018, **140**, 2085-2092.
160. R. K. Yadav, A. Kumar, N. J. Park, K. J. Kong and J. O. Baeg, *Journal of Materials Chemistry A*, 2016, **4**, 9413-9418.
161. Z. Y. Fan, K. Nomura, M. S. Zhu, X. X. Li, J. W. Xue, T. Majima and Y. Osakada, *Commun Chem*, 2019, **2**, 55.
162. Y. C. Yuan, B. Sun, A. M. Cao, D. Wang and L. J. Wan, *Chem Commun*, 2018, **54**, 5976-5979.
163. H. Yang, X. P. Cheng, X. X. Cheng, F. S. Pan, H. Wu, G. H. Liu, Y. M. Song, X. Z. Cao and Z. Y. Jiang, *Journal of Membrane Science*, 2018, **565**, 331-341.
164. X. Zhang, Z. Wang, L. Yao, Y. Y. Mai, J. Q. Liu, X. L. Hua and H. Wei, *Materials Letters*, 2018, **213**, 143-147.
165. W. Huang, Z. J. Wang, B. C. Ma, S. Ghasimi, D. Gehrig, F. Laquai, K. Landfester and K. A. I. Zhang, *Journal of Materials Chemistry A*, 2016, **4**, 7555-7559.
166. B. Gole, V. Stepanenko, S. Rager, M. Grune, D. D. Medina, T. Bein, F. Wurthner and F. Beuerle, *Angew Chem Int Edit*, 2018, **57**, 846-850.
167. S. Kandambeth, V. Venkatesh, D. B. Shinde, S. Kumari, A. Halder, S. Verma and R. Banerjee, *Nature communications*, 2015, **6**, 6786.
168. C. Qian, S. Q. Xu, G. F. Jiang, T. G. Zhan and X. Zhao, *Chem-Eur J*, 2016, **22**, 17784-17789.
169. T.-Y. Zhou, F. Lin, Z.-T. Li and X. Zhao, *Macromolecules*, 2013, **46**, 7745-7752.
170. J. B. Joo, Q. Zhang, I. Lee, M. Dahl, F. Zaera and Y. J. Yin, *Adv Funct Mater*, 2012, **22**, 166-174.
171. C. C. Nguyen, N. N. Vu and T. O. Do, *Journal of Materials Chemistry A*, 2015, **3**, 18345-18359.
172. H. X. Li, Z. F. Bian, J. Zhu, D. Q. Zhang, G. S. Li, Y. N. Huo, H. Li and Y. F. Lu, *J Am Chem Soc*, 2007, **129**, 8406-8407.
173. Z. Wang, J. G. Hou, C. Yang, S. Q. Zhao, K. Huang and H. M. Zhu, *Energy & Environmental Science*, 2013, **6**, 2134-2144.
174. H. X. Guo, J. H. Wang, Q. F. Fang, Y. Zhao, S. Gu, J. Zheng and Y. S. Yan, *Crystengcomm*, 2017, **19**, 4905-4910.
175. Q. Gao, X. Li, G. H. Ning, K. Leng, B. B. Tian, C. B. Liu, W. Tang, H. S. Xu and K. P. Loh, *Chem Commun*, 2018, **54**, 2349-2352.
176. J. Q. Dong, Y. X. Wang, G. L. Liu, Y. D. Cheng and D. Zhao, *Crystengcomm*, 2017, **19**, 4899-4904.
177. L. H. Li, X. L. Feng, X. H. Cui, Y. X. Ma, S. Y. Ding and W. Wang, *J Am Chem Soc*, 2017, **139**, 6042-6045.
178. G. H. Ning, Z. X. Chen, Q. Gao, W. Tang, Z. X. Chen, C. B. Liu, B. B. Tian, X. Li and K. P. Loh, *J Am Chem Soc*, 2017, **139**, 8897-8904.
179. S. Bi, C. Yang, W. B. Zhang, J. S. Xu, L. M. Liu, D. Q. Wu, X. C. Wang, Y. Han, Q. F. Liang and F. Zhang, *Nature communications*, 2019, **10**, 2467.
180. M. L. Luo, Q. Yang, K. W. Liu, H. M. Cao and H. J. Yan, *Chem Commun*, 2019, **55**, 5829-5832.
181. L. Stegbauer, S. Zech, G. Savasci, T. Banerjee, F. Podjaski, K. Schwinghammer, C. Ochsenfeld and B. V. Lotsch, *Adv Energy Mater*, 2018, **8**, 1703278.
182. W. B. Chen, Z. F. Yang, Z. Xie, Y. S. Li, X. Yu, F. L. Lu and L. Chen, *Journal of Materials Chemistry A*, 2019, **7**, 998-1004.
183. W. Huang, Q. He, Y. P. Hu and Y. G. Li, *Angew Chem Int Edit*, 2019, **58**, 8676-8680.
184. S. Ghosh, N. A. Kouame, L. Ramos, S. Remita, A. Dazzi, A. Deniset-Besseau, P. Beauvier, F. Goubard, P. H. Aubert and H. Remita, *Nature materials*, 2015, **14**, 505-511.
185. C. C. Wang, Y. Guo, Y. Yang, S. Chu, C. K. Zhou, Y. Wang and Z. G. Zou, *ACS applied materials & interfaces*, 2014, **6**, 4321-4328.
186. J. H. Li, B. A. Shen, Z. H. Hong, B. Z. Lin, B. F. Gao and Y. L. Chen, *Chem Commun*, 2012, **48**, 12017-12019.
187. Z. Cheng, K. Y. Zheng, G. Y. Lin, S. Q. Fang, L. Y. Li, J. H. Bi, J. N. Shen and L. Wu, *Nanoscale Adv*, 2019, **1**, 2674-2680.
188. R. Xu, X. S. Wang, H. Zhao, H. Lin, Y. B. Huang and R. Cao, *Catal Sci Technol*, 2018, **8**, 2224-2230.
189. Y. M. Zhang, Y. M. Hu, J. H. Zhao, E. Park, Y. H. Jin, Q. J. Liu and W. Zhang, *Journal of Materials Chemistry A*, 2019, **7**, 16364-16371.
190. J. Chen, X. P. Tao, L. Tao, H. Li, C. Z. Li, X. L. Wang, C. Li, R. G. Li and Q. H. Yan, *Appl Catal B-Environ*, 2019, **241**, 461-470.
191. J. Di, J. X. Xu, H. M. Li, S. J. Guo and S. Dai, *Nano Energy*, 2017, **40**, 172-182.
192. L. Zhang, W. Z. Wang, S. M. Sun, Y. Y. Sun, E. P. Gao and J. Xu, *Appl Catal B-Environ*, 2013, **132**, 315-320.
193. Y. Y. Ding, P. L. Wang, G. L. Yin, X. Q. Zhang and G. X. Lu, *International Journal of Hydrogen Energy*, 2019, **44**, 11872-11879.
194. S. Pandey, S. Kandambeth, D. D. Diaz and R. Banerjee, *Chem Commun*, 2014, **50**, 3169-3172.
195. S. Thote, H. B. Aiyappa, A. Deshpande, D. D. Diaz, S. Kurungot and R. Banerjee, *Chem-Eur J*, 2014, **20**, 15961-15965.
196. D. K. Wang, X. Li, L. L. Zheng, L. M. Qin, S. Li, P. Ye, Y. Li and J. P. Zou, *Nanoscale*, 2018, **10**, 19509-19516.
197. S. R. Zhu, M. K. Wu, W. N. Zhao, F. Y. Yi, K. Tao and L. Han, *J Solid State Chem*, 2017, **255**, 17-26.
198. J. Li, Y. Yu and L. Z. Zhang, *Nanoscale*, 2014, **6**, 8473-8488.
199. S. R. Zhu, Q. Qi, Y. Fang, W. N. Zhao, M. K. Wu and L. Han, *Cryst Growth Des*, 2018, **18**, 883-891.
200. Y. W. Peng, M. T. Zhao, B. Chen, Z. C. Zhang, Y. Huang, F. N. Dai, Z. C. Lai, X. Y. Cui, C. L. Tan and H. Zhang, *Advanced materials*, 2018, **30**, 1705454.
201. S. S. Yi, J. M. Yan, B. R. Wulan, S. J. Li, K. H. Liu and Q. Jiang, *Appl Catal B-Environ*, 2017, **200**, 477-483.
202. M. Zheng, Y. Ding, L. Yu, X. Q. Du and Y. K. Zhao, *Adv Funct Mater*, 2017, **27**, 1605846.
203. C. B. Meier, R. S. Sprick, A. Monti, P. Guiglion, J. S. M. Lee, M. A. Zwiijnenburg and A. I. Cooper, *Polymer*, 2017, **126**, 283-290.
204. D. Wang, H. Zeng, X. Xiong, M.-F. Wu, M. Xia, M. Xie, J.-P. Zou and S.-L. Luo, *Science Bulletin*, 2019, DOI: 10.1016/j.scib.2019.10.015.
205. S. Kuecken, A. Acharyya, L. J. Zhi, M. Schwarze, R. Schomacker and A. Thomas, *Chem Commun*, 2017, **53**, 5854-5857.
206. L. P. Guo, Y. L. Niu, S. Razzaque, B. Tan and S. B. Jin, *Acs Catal*, 2019, **9**, 9438-9445.
207. T. Ishi-i, K. Yaguma, T. Thiemann, M. Yashima, K. Ueno and S. Mataka, *Chem Lett*, 2004, **33**, 1244-1245.

208. R. S. Sprick, B. Bonillo, R. Clowes, P. Guiglion, N. J. Brownbill, B. J. Slater, F. Blanc, M. A. Zwiijnenburg, D. J. Adams and A. I. Cooper, *Angew Chem Int Edit*, 2016, **55**, 1824-1828.
209. J. L. Sheng, H. Dong, X. B. Meng, H. L. Tang, Y. H. Yao, D. Q. Liu, L. L. Bai, F. M. Zhang, J. Z. Wei and X. J. Sun, *Chemcatchem*, 2019, **11**, 2313-2319.
210. F. Li, D. K. Wang, Q. J. Xing, G. Zhou, S. S. Liu, Y. Li, L. L. Zheng, P. Ye and J. P. Zou, *Appl Catal B-Environ*, 2019, **243**, 621-628.
211. J. H. Yang, D. G. Wang, H. X. Han and C. Li, *Accounts Chem Res*, 2013, **46**, 1900-1909.
212. W. T. Eckenhoff, W. R. McNamara, P. W. Du and R. Eisenberg, *Bba-Bioenergetics*, 2013, **1827**, 958-973.
213. P. W. Du and R. Eisenberg, *Energy & Environmental Science*, 2012, **5**, 6012-6021.
214. J. He, L. Chen, F. Wang, Y. Liu, P. Chen, C. T. Au and S. F. Yin, *ChemSusChem*, 2016, **9**, 624-630.
215. X. Q. Hao, Z. L. Jin, H. Yang, G. X. Lu and Y. P. Bi, *Appl Catal B-Environ*, 2017, **210**, 45-56.
216. Q. Q. Jiang, L. Sun, J. H. Bi, S. J. Liang, L. Y. Li, Y. Yu and L. Wu, *ChemSusChem*, 2018, **11**, 1108-1113.
217. J. L. Dempsey, B. S. Brunschwig, J. R. Winkler and H. B. Gray, *Accounts Chem Res*, 2009, **42**, 1995-2004.
218. T. Banerjee, F. Haase, G. Savasci, K. Gottschling, C. Ochsenfeld and B. V. Lotsch, *J Am Chem Soc*, 2017, **139**, 16228-16234.
219. J. W. Tang, J. R. Durrant and D. R. Klug, *J Am Chem Soc*, 2008, **130**, 13885-13891.
220. Z. A. Lan, Y. X. Fang, Y. F. Zhang and X. C. Wang, *Angew Chem Int Edit*, 2018, **57**, 470-474.
221. D. Kong, X. Y. Han, J. J. Xie, Q. S. Ruan, C. D. Windle, S. Gadipelli, K. Shen, Z. M. Bai, Z. X. Guo and J. W. Tang, *Adv Catal*, 2019, **9**, 7697-7707.
222. E. Jin, Z. Lan, Q. Jiang, K. Geng, G. Li, X. Wang and D. Jiang, *Chem*, 2019, **5**, 1632-1647.
223. J. Chen, X. P. Tao, C. Z. Li, Y. H. Ma, L. Tao, D. Y. Zheng, J. F. Zhu, H. Li, R. G. Li and Q. H. Yang, *Appl Catal B-Environ*, 2020, **262**, 118271.
224. A. Dhakshinamoorthy, S. Navalon, A. Colma and H. Garcia, *Energy & Environmental Science*, 2013, **6**, 9217-9233.
225. M. Bui, C. S. Adjiman, A. Bardow, E. J. Anthony, A. Boston, S. Brown, P. S. Fennell, S. Fuss, A. Galindo, L. A. Hackett, J. P. Hallett, H. J. Herzog, G. Jackson, J. Kemper, S. Krevor, G. C. Maitland, M. Matuszewski, I. S. Metcalfe, C. Petit, G. Puxty, J. Reimer, D. M. Reiner, E. S. Rubin, S. A. Scott, N. Shah, B. Smit, J. P. M. Trusler, P. Webley, J. Wilcox and N. Mac Dowell, *Energy & Environmental Science*, 2018, **11**, 1062-1176.
226. W. G. Tu, Y. Zhou and Z. G. Zou, *Adv Funct Mater*, 2013, **23**, 4996-5008.
227. D. M. D'Alessandro, B. Smit and J. R. Long, *Angew Chem Int Edit*, 2010, **49**, 6058-6082.
228. F. Fresno, R. Portela, S. Suarez and J. M. Coronado, *Journal of Materials Chemistry A*, 2014, **2**, 2863-2884.
229. A. J. Cowan and J. R. Durrant, *Chemical Society reviews*, 2013, **42**, 2281-2293.
230. W. L. Yu, D. F. Xu and T. Y. Peng, *Journal of Materials Chemistry A*, 2015, **3**, 19936-19947.
231. T. M. Di, B. C. Zhu, B. Cheng, J. G. Yu and J. S. Xu, *J Catal*, 2017, **352**, 532-541.
232. M. Lu, Q. Li, J. Liu, F. M. Zhang, L. Zhang, J. L. Wang, Z. H. Kang and Y. Q. Lan, *Appl Catal B-Environ*, 2019, **254**, 624-633.
233. J. L. White, M. F. Baruch, J. E. Pander, Y. Hu, I. C. Fortmeyer, J. E. Park, T. Zhang, K. Liao, J. Gu, Y. Yan, T. W. Shaw, E. Abelev and A. B. Bocarsly, *Chemical reviews*, 2015, **115**, 12888-12935.
234. J. Agarwal, E. Fujita, H. F. Schaefer and J. T. Muckerman, *J Am Chem Soc*, 2012, **134**, 5180-5186.
235. W. F. Zhong, R. J. Sa, L. Y. Li, Y. J. He, L. Y. Li, J. H. Bi, Z. Y. Zhuang, Y. Yu and Z. G. Zou, *J Am Chem Soc*, 2019, **141**, 7615-7621.
236. S. Y. Li, S. Meng, X. Q. Zou, M. El-Roz, I. Teleguev, O. Thili, T. X. Liu and G. S. Zhu, *Micropor Mesopor Mat*, 2019, **285**, 195-201.
237. P. D. C. Dietzel, R. E. Johnsen, H. Fjellvag, S. Bordiga, E. Groppo, S. Chavan and R. Blom, *Chem Commun*, 2008, DOI: 10.1039/b810574j, 5125-5127.
238. J. J. Zhang, H. Wang, X. Z. Yuan, G. M. Zeng, W. G. Tu and S. B. Wang, *J Photoch Photobio C*, 2019, **38**, 1-26.
239. H. Yi, M. Yan, D. J. Huang, G. M. Zeng, C. Lai, M. F. Li, X. Q. Huo, L. Qin, S. J. Liu, X. G. Liu, B. S. Li, H. Wang, M. C. Shen, Y. K. Fu and Y. Guo, *Appl Catal B-Environ*, 2019, **250**, 52-62.
240. R. Jaiswal, M. Patel, A. Dashora, R. Fernandes, M. Yadav, R. Edla, R. S. Varma, D. C. Kothari, B. L. Ahuja and A. Miotello, *Appl Catal B-Environ*, 2016, **183**, 242-253.
241. H. Safajou, H. Khojasteh, M. Salavati-Niasari and S. Mortazavi-Derazkola, *J Colloid Interf Sci*, 2017, **498**, 423-432.
242. J. X. Low, J. G. Yu, M. Jaroniec, S. Wageh and A. A. Al-Shamdi, *Advanced materials*, 2017, **29**, 1601694.
243. C. Y. Wang, Y. J. Zhang, W. K. Wang, D. N. Pei, G. X. Huang, J. J. Chen, X. Zhang and H. Q. Yu, *Appl Catal B-Environ*, 2018, **221**, 320-328.
244. Y. Mi, L. Y. Wen, Z. J. Wang, D. W. Cao, R. Xu, Y. G. Fang, Y. L. Zhou and Y. Lei, *Nano Energy*, 2016, **30**, 109-117.
245. F. L. Wang, P. Chen, Y. P. Feng, Z. J. Xie, Y. Liu, Y. H. Su, Q. X. Zhang, Y. F. Wang, K. Yao, W. Y. Lv and G. G. Liu, *Appl Catal B-Environ*, 2017, **207**, 103-113.
246. N. Xu, R. L. Wang, D. P. Li, X. Meng, J. L. Mu, Z. Y. Zhou and Z. M. Su, *Dalton T*, 2018, **47**, 4191-4197.
247. F. Niu, L. M. Tao, Y. C. Deng, H. Gao, J. G. Liu and W. G. Song, *New J Chem*, 2014, **38**, 5695-5699.
248. S. J. He, Q. F. Rong, H. Y. Niu and Y. Q. Cai, *Chem Commun*, 2017, **53**, 9636-9639.
249. X. L. Yang, F. F. Qian, G. J. Zou, M. L. Li, J. R. Lu, Y. M. Li and M. T. Bao, *Appl Catal B-Environ*, 2016, **193**, 22-35.
250. S. M. Wang, D. L. Li, C. Sun, S. G. Yang, Y. Guan and H. He, *Appl Catal B-Environ*, 2014, **144**, 885-892.
251. S. Kumar, A. Baruah, S. Tonda, B. Kumar, V. Shanker and B. Sreedhar, *Nanoscale*, 2014, **6**, 4830-4842.
252. S. J. He, B. Yin, H. Y. Niu and Y. Q. Cai, *Appl Catal B-Environ*, 2018, **239**, 147-153.
253. Q. H. Liang, Z. Li, Z. H. Huang, F. Y. Kang and Q. H. Yang, *Adv Funct Mater*, 2015, **25**, 6885-6892.
254. J. Q. Pan, L. P. Guo, S. Q. Zhang, N. Wang, S. B. Jin and B. Tan, *Chem-Asian J*, 2018, **13**, 1674-1677.
255. K. Preet, G. Gupta, M. Kota, S. K. Kansal, D. B. Salunke, H. K. Sharma, S. C. Sahoo, P. Van der Voort and S. Roy, *Cryst Growth Des*, 2019, **19**, 2525-2530.



256. W. N. Wang, W. J. An, B. Ramalingam, S. Mukherjee, D. M. Niedzwiedzki, S. Gangopadhyay and P. Biswas, *J Am Chem Soc*, 2012, **134**, 11276-11281.
257. C. T. Dinh, H. Yen, F. Kleitz and T. O. Do, *Angew Chem Int Edit*, 2014, **53**, 6618-6623.
258. S. J. He, Q. F. Rong, H. Y. Niu and Y. Q. Cai, *Appl Catal B-Environ*, 2019, **247**, 49-56.
259. S. Gu, S. F. Wu, L. J. Cao, M. C. Li, N. Qin, J. Zhu, Z. Q. Wang, Y. Z. Li, Z. Q. Li, J. J. Chen and Z. G. Lu, *J Am Chem Soc*, 2019, **141**, 9623-9628.
260. X. W. Wu, X. Han, Q. S. Xu, Y. H. Liu, C. Yuan, S. Yang, Y. Liu, J. W. Jiang and Y. Cui, *J Am Chem Soc*, 2019, **141**, 7081-7089.
261. A. K. Beine, A. J. D. Kruger, J. Artz, C. Weidenthaler, C. Glotzbach, P. J. C. Hausoul and R. Palkovits, *Green Chem*, 2018, **20**, 1316-1322.
262. Y. J. Li, S. H. Zheng, X. Liu, P. Li, L. Sun, R. X. Yang, S. Wang, Z. S. Wu, X. H. Bao and W. Q. Deng, *Angew Chem Int Edit*, 2018, **57**, 7992-7996.
263. H. Wei, S. Z. Chai, N. T. Hu, Z. Yang, L. M. Wei and L. Wang, *Chem Commun*, 2015, **51**, 12178-12181.
264. S. J. Ren, M. J. Bojdys, R. Dawson, A. Laybourn, Y. Z. Khimyak, D. J. Adams and A. I. Cooper, *Advanced materials*, 2012, **24**, 2357-2361.
265. G. Lin, C. H. Gao, Q. Zheng, Z. X. Lei, H. J. Geng, Z. Lin, H. H. Yang and Z. W. Cai, *Chem Commun*, 2017, **53**, 3649-3652.
266. Y. W. Peng, W. K. Wong, Z. G. Hu, Y. D. Cheng, D. Q. Yuan, S. A. Khan and D. Zhao, *Chemistry of Materials*, 2016, **28**, 5095-5101.
267. R. Chen, Z. H. Yan, X. J. Kong, L. S. Long and L. S. Zheng, *Angew Chem Int Edit*, 2018, **57**, 16796-16800.
268. W. Y. Lu, T. F. Xu, Y. Wang, H. G. Hu, N. Li, X. M. Jiang and W. X. Chen, *Appl Catal B-Environ*, 2016, **180**, 20-28.
269. C. Krishnaraj, A. M. Kaczmarek, H. S. Jena, K. Leus, M. Chaoui, J. Schmidt, R. Van Deun and P. Van der Voort, *ACS applied materials & interfaces*, 2019, **11**, 27343-27352.
270. J. H. Bi, W. Fang, L. Y. Li, J. Y. Wang, S. J. Liang, Y. H. Hu, M. H. Liu and L. Wu, *Macromolecular Rapid Communications*, 2015, **36**, 1799-1805.

Accepted MS